Skin-Friction Measurement on a Flexible Membrane Using Oil Film Interferometry

A Thesis

Presented in Partial Fulfillment of the Requirements for the

Degree of Master of Science

with a

Major in Mechanical Engineering

in the

College of Graduate Studies

University of Idaho

by

Kirk D. McKenzie

Approved by:

Major Professor: Vibhav Durgesh, Ph.D.

Committee Members: John Crepeau, Ph.D.; Tao Xing, Ph.D.

Department Administrator: Gabriel Potirniche, Ph.D.

August 2022

Abstract

Fluid-structure-interactions (FSI) has applications in diverse areas and has been a research focus for several decades. FSI is used in studying aerodynamics and can be observed from a flag flapping in the wind, or a parachute deploying. The nonlinear coupling between a structure and fluid flow makes computational and theoretical studies challenging. One of the critical fluid dynamic parameters of FSI research is skin-friction coefficient (C_f), a dimensionless parameter used to determine viscous drag on a structure. An accurate estimation of C_f can provide critical information regarding FSI physics and aid in developing robust computational and theoretical models. Furthermore, traditional experimental approaches to measure C_f are intrusive and can alter the fluid flow field and structure properties. One such traditional method being a Stanton tube, where the tube is placed close to the structure surface to collect pressure differences, in turn obstructing the flow near the structure. Another method being a Micro Electrical Mechanical System (MEMS) sensor, a reliable method that requires contact with the surface, influencing the behavior of the structure. This study aims to design and develop an optical-based C_f measurement technique (i.e., Oil-Film-Interferometry (OFI)) that is non-intrusive and can be used to estimate values on a very flexible and transparent membrane. For this purpose, an in-house OFI system was designed by creating a 3-D printed model that negates pressure gradients at the leading edge of a flat plate. The OFI system was used to perform experiments on a flat plate model in the wind tunnel facility at the University of Idaho's Experimental Fluids and Aerodynamics Laboratory (EFAL). In-plane image analysis of oil fringe patterns were achieved by process of photogrammetry, which mapped a 3-D space to a 2-D image plane. After image correction, a Windowed Fourier Transform (WFT) approach was used to analyze fringe spacing that led to determination of the local oil height that is used to iteratively solve for C_f . The OFI technique successfully measured C_f on a flat plate model and yielded a deviation within 6% from theoretical results. After a successful demonstration in the wind tunnel, the in-house OFI system was designed to measure skin friction on a flexible membrane model using the open jet facility in EFAL. The OFI results on the flexible membrane yielded a deviation within 8% of theoretical C_f results over a flat plate. This study successfully demonstrated the application of the OFI technique to measure C_f on flexible transparent structures. Performing OFI to measure the skin friction coefficient on a flexible membrane has provided a new approach to accurately characterize wall shear stresses on a flexible structure, setting the foundation for future work in which OFI measurements will be taken on a flexible membrane with various modes of oscillation.

Acknowledgements

I would like to thank the following for their support in obtaining my degree:

Dr. Vibhav Durgesh - My advisor - For passing down knowledge, lending advice and guidance on how to properly conduct my experiments and analyze my work to achieve success.

Dr. Paulo Yu, Rodrigo Padilla and Piyush Basnet - My lab partners - For exchanging ideas, sharing opinions, and providing good company in the lab.

Dedication

For my mother Monique, my father David, my sister Lauren and brother Cade, along with all of my extended family and friends who provided me with endless love and support.

Table of Contents

List of Tables

List of Figures

List of Acronyms

c	principle distance
C_f	skin friction coefficient
δ	boundary layer thickness
δ^*	boundary layer displacement thickness
E	average output voltage
E_p	precision error
F	focal length
h	oil film thickness
K	camera intrinsic matrix
k	fringe number
λ	illumination wavelength
n	local streamline divergence
p	pressure
ϕ	phase difference
q	dynamic pressure
R	rotation matrix
$R_{i,i}$	auto correlation value
Re_x	Reynolds number
ρ	density of the fluid
$\rho_{i,if}$	cross correlation coefficient
t	time
TI	turbulence intensity
τ_w	wall shear-stress
θ	momentum thickness
θ_i	incidence angle of light
u	x-component of velocity

U	upstream velocity
U_∞	free-stream velocity
ν	kinematic viscosity
μ	dynamic viscosity
v	y-component of velocity

Chapter 1: Introduction

1.1 Overview

The study of fluid structure interactions (FSI) is a growing area of interest in the fluid dynamics community. FSI couples the behavior of fluid flow over a structure, as well as the behavior of the structure that is subject to a fluid flow. Some examples of this behavior are observed in bio-propulsion, such as that of a fish swimming [Ehrenstein et al., 2014] or thrust generated by a bird's wing [Vandenberghe et al., 2006]. Other common examples of FSI include a flag flapping in the wind [Goza and Colonius, 2018], the wing of an airplane [Son et al., 2016], and a parachute deploying [Takizawa et al., 2013]. The coupling between the fluid flow and structure presents a non-linear problem that is difficult to analytically solve.

Controlled experiments and idealized numerical models are used to understand the physics and mechanics of FSI behavior. The shape, rigidity, size and orientation of the structure relative to the fluid velocity are key wall shear stress parameters in setting up an FSI model. To quantify wall shear stress, the boundary layer over a solid and static body has been rigorously studied. A commonly used non-dimensional parameter to quantify wall shear stress is the skin friction coefficient which is used to solve for friction drag. In this study, the skin friction coefficient is measured on a flexible membrane.

Skin friction measurement on a flexible membrane is challenging due to the structure moving dynamically in the presence of fluid flow, and inability to attach a sensor to the flexible membrane. Numerical models and simulations require predetermined flow conditions to solve for skin friction, such as structure shape, roughness, type of flow, and mesh criteria. This raises a challenge because FSI, in many cases, contains natural and random behaviors that may not agree with these predetermined conditions in a simulation. Experiments that measure skin friction is intrusive and can impact the flow, structure, or both, adding uncertainty in the measurement. An optical based, non-intrusive skin friction measurement technique may lead to overcoming these challenges.

Skin friction values provide crucial information regarding wall shear stress, and can help in identifying optimal geometric shape, orientation and material of a body that endures fluid flow. Flexible structures have recently been gaining more attention as advancements in technology has transitioned the aerospace industry to designs involving flexible bodies and materials. Benefits of flexible materials include weight and size reduction, along with the ability to compact the material before it is used. A key example is NASA's Deployable Hypersonic Inflatable Aerodynamic Decelerator (HIAD). This design utilizes inflatable, flexible materials that are deployed into a large aeroshell upon atmospheric entry on martian planets. It consists of pressurized concentric tubes that are braided synthetic fibers 15 times the strength

of steel [Vitug, 2020]. These fibers are able to withstand the high-energy drag forces that a spacecraft encounters during atmospheric entry.

Oil film interferometry (OFI) is an indirect technique to measure wall shear stress and derive a local skin friction coefficient. [Squire, 1961] first recognized the relationship between the height of an oil film subject to flow and the corresponding shear stress. This relationship was further developed by [Tanner and Blows, 1976] and was applied to a surface to measure shear stress. Since then, a multitude of studies [Tanner, 1979, Monson et al., 1993, Zilliac, 1996, Naughton et al., 2001, Decker and Naughton, 2001] have expanded on this idea and applied it to various models and testing conditions. OFI is a relatively simple yet accurate technique to estimate skin friction values, and can be applied to a wide variety of complex flows. This study aims to create a measurement system to quantify the skin friction coefficient on a flexible membrane subject to fluid flow.

An oil film fringe pattern is a produced by constructive and destructive interferences of light reflecting off surface where the oil is placed. To visually observe and analyze these fringe patterns, a light source and reflective surface is required to be captured by a camera. The most common applications being a mirror polished steel plate, or a solid model wrapped in a reflective material such as Mylar. The ability to advance on this measurement technique and apply OFI to a transparent, flexible membrane has yet to be conducted. The determination of skin friction and wall shear stresses over a flexible body further solidifies the understanding of structural behaviors and the corresponding boundary layer profile.

1.2 Objective

There were three main objectives for this study. The first was to quantify the velocity profile for the wind tunnel test section at the University of Idaho's Experimental Fluids and Aerodynamics Lab (EFAL). The purpose of this is to understand the uniformity of different flow conditions at different heights within the test section. The second objective was to validate OFI measurements and analysis techniques in the wind tunnel. This provided confidence in applying these methods to more OFI experiments using different test parameters. Third was to quantify skin friction values on a flexible membrane using EFAL's open jet facility. In future experimental and analysis techniques, the methods developed here will serve as a foundation for future skin friction measurements on a flexible membrane. This was the first recorded occurrence of performing OFI to derive skin friction coefficients on a thin, transparent, flexible membrane.

Objectives of this study were achieved by performing the following experiments and data analysis. Hot wire anemometry (HWA) tests were performed at different locations in the wind tunnel. The results provided local velocities at the locations measured. A velocity profile of the wind tunnel was derived to analyze the flow conditions as a function of height. Next, OFI was performed on a flat plate within the

wind tunnel. Resulting skin friction coefficients and wall shear stress values were compared with known theoretical results to validate the measurement technique and fringe analysis approach. The results are in good agreement with theory of flow over a flat plate, concluding that the technique and approach are of valid for use of further experiments. OFI was then performed on a thin, transparent, flexible membrane using the jet facility at EFAL. For validation of these results, skin friction and wall shear stress values were again compared to theory of flow over a flat plate. The results show a link between the flexible membrane and flat plate components when subjected to laminar flow. Compiling this work provides a foundation for measurement and analysis standards for skin friction measurements on a flexible membrane. These standards will be applied in future studies at EFAL regarding turbulent regimes of fluid flow around the flexible membrane.

The following chapters provide background studies and governing equations of the experimental and analysis techniques that are applied in this study. Next, the experimental setups and instrumentation used in this study are highlighted. The approach follows, providing detail on how the experimental data is processed, as well as uncertainties relating to this study. Finally, the results are discussed, summarized and concluded upon.

Chapter 2: Background

2.1 Boundary Layer Characteristics and Wall Shear Stress

Boundary layer studies have been a foundation of fluid dynamics in modern history. Ludwig Prandtl (1875-1953) developed modern boundary layer theory, and is widely considered to be the father of present-day fluid dynamics. One of his students, Paul Blasius (1883-1970), provided an analytic solution to the boundary layer equations [Munson et al., 2013] [Ch. 9]. The quantification of boundary layer characteristics are critical to understanding the behavior of a structure that is subject to fluid flow. Theory for a boundary layer observed over a flat plate is well documented in both experimental and simulated studies in fluid flow over a body. Blasius derived a modern solution to the boundary layer of flow parallel to a flat plate [White, 1974]. Here, a brief overview will be provided.

A boundary layer is defined as a thin layer near any fixed surface in a moving stream in which viscous shearing stresses are not negligible [Munson et al., 2013]. Shearing stresses develop in a fluid that is subject to movement because of the fluid's viscosity. The boundary layer thickness (δ) is the distance from the surface at which the x-component of velocity (u) of the fluid is within 99% of the of the upstream velocity (U) and is given by

$$\delta = y \quad \text{and} \quad u = 0.99U, \tag{2.1}$$

in reference to Figure 2.1. The definition of $u = 0.99U$ is arbitrary as 90% and 95% also exist. However, this definition is useful in defining the extent of the velocity boundary layer at the surface.

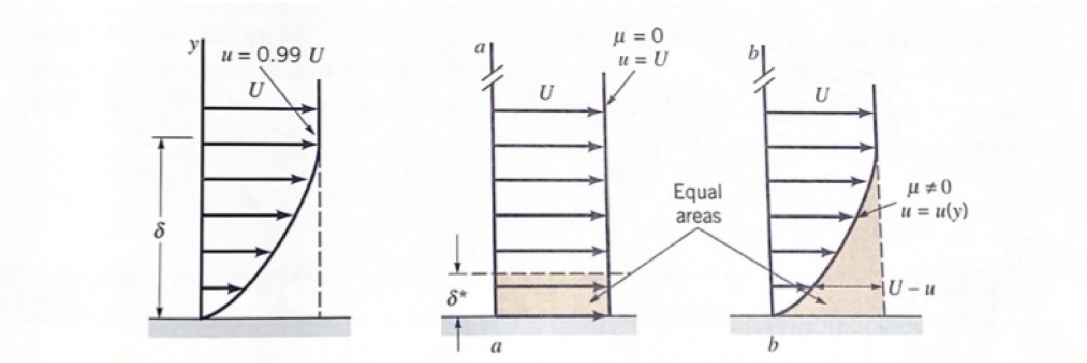

Figure 2.1: Boundary layer thickness and displacement thickness. From [Munson et al., 2013].

The boundary layer displacement thickness (δ^*) in 2.1, is the amount that the thickness of the boundary layer must be increased by so the inviscid uniform flow has the same properties as the viscous flow, and

is given by

$$\delta^* = \int_0^\infty \left(1 - \frac{u}{U}\right) dy. \tag{2.2}$$

The displacement thickness represents the outward displacement of the streamlines caused by viscous effects on the plate. This helps simulate the effect that the boundary layer has on the flow, outside the boundary layer itself, by modeling δ^* as an additive to the surface and treating the flow over the surface as inviscid flow.

Another key boundary layer characteristic is the momentum thickness (θ). This is crucial when determining the drag on an object and is given by

$$\theta = \int_0^\infty \frac{u}{U}\left(1 - \frac{u}{U}\right) dy. \tag{2.3}$$

In a physical sense, θ means the shear stress at the surface is equal to the gain of momentum in the boundary layer [Sakiadis, 1961]. Futhermore, it is defined in relation to the momentum flow rate within the boundary layer. This flow rate is less than the rate that would occur if no boundary layer existed (i.e. $u = U$) [Houghton and Carpenter, 2003].

2.2 Flat Plate Laminar Boundary Layer

Flow past any object that is viscous and imcompressible can be solved using the Navier-Stokes equations discussed in [Doering and Gibbon, 1995, Munson et al., 2013]. Prandtl was able to simplify these equations by implying certain approximations over a flat plate. For a steady, two-dimensional laminar flow with negligible gravitational effects, the Navier-Stokes equations reduce to

$$u\frac{\partial u}{\partial x} + v\frac{\partial u}{\partial y} = -\frac{1}{\rho}\frac{\partial p}{\partial x} + \nu\left(\frac{\partial^2 u}{\partial x^2} + \frac{\partial^2 u}{\partial y^2}\right), \tag{2.4}$$

$$u\frac{\partial v}{\partial x} + v\frac{\partial v}{\partial y} = -\frac{1}{\rho}\frac{\partial p}{\partial y} + \nu\left(\frac{\partial^2 v}{\partial x^2} + \frac{\partial^2 v}{\partial y^2}\right), \tag{2.5}$$

where the variables are defined as the x-component of velocity (u), the y-component of velocity (v), using the coordinate system defined in figure 2.1, density of the fluid (ρ), pressure (p), and kinematic viscosity (ν). Conservation of mass of incompressible flow leads to

$$\frac{\partial u}{\partial x} + \frac{\partial v}{\partial y} = 0. \tag{2.6}$$

Blasius was then able to solve Equations 2.4 and 2.5 for boundary layer flow past a flat plate parallel to the flow field. Assumptions were made on the fact that the boundary layer is thin, which leads to the conclusion that velocity component normal to the flow will be much smaller than the component parallel to the flow, that is

$$u \gg v. \tag{2.7}$$

Furthermore, the rate of change of any parameter across the boundary layer is expected to be much greater than that along the flow direction meaning

$$\frac{\partial}{\partial y} \gg \frac{\partial}{\partial x} \tag{2.8}$$

Applying these assumptions to Equations 2.4, 2.5 and 2.6 reduce the boundary layer solution across a flat plate to

$$\frac{\partial u}{\partial x} + \frac{\partial v}{\partial y} = 0, \tag{2.9}$$

$$u\frac{\partial u}{\partial x} + v\frac{\partial v}{\partial y} = \nu\frac{\partial^2 u}{\partial y^2}. \tag{2.10}$$

The wall shear-stress (τ_w) acting on the plate is dependent on both the dynamic viscosity (μ) of the fluid and the velocity profile shown in Equations 2.9 and 2.10, and is given by

$$\tau_w = \mu \left(\frac{\partial u}{\partial y}\right)_{y=0}, \tag{2.11}$$

where the velocity gradient is evaluated at the plate. Moreover, the local skin friction coefficient (C_f) is the ratio of momentum thickness θ and displacement along the plate, x, shown in Equation 2.12. Wall shear stress is often expressed in the terms of the dimensionless local skin coefficient and is given by

$$C_f = \frac{\tau_w}{\frac{1}{2}\rho U^2} = \frac{\theta}{x}. \tag{2.12}$$

Skin friction parameters over a flat plate are discussed here in a general form, for further detailed information and derivations, see [White, 1974] [Ch. 4-6] [Munson et al., 2013, Doering and Gibbon, 1995, Sakiadis, 1961]. When analyzing a fluid as a function of distance along a surface, a dimensionless parameter relating fluid properties and displacement is needed. The Reynolds number (Re_x) can serve as this relationship and is given by

$$Re_x = \frac{\rho U x}{\mu}, \tag{2.13}$$

where ρ is the fluid density, U is the fluid velocity, x is the distance along the plate, and μ is the dynamic viscosity of the fluid. The Blasius solution for C_f in terms of Re_x is a modified version of Equation 2.12 and is given by

$$C_f = \frac{0.664}{\sqrt{Re_x}}. \tag{2.14}$$

Turbulent flows add a significant level of complexity to the solution for a flat plate. A larger velocity gradient is observed at the surface, as well as a larger boundary layer thickness. An exact solution for turbulent boundary layer flow does not exist. However, parametric relations performed by Prandtl and Blasius correlated wall shear stress behavior in a pipe to the local shear stress on a plate. The parametric relation for C_f, when neglecting the law of the outer wake, is given by

$$C_f = \frac{0.027}{Re_x^{\frac{1}{7}}}. \tag{2.15}$$

The wall shear stress determines how a surface and fluid interact with one another. When predicting or modeling the boundary layer for an FSI problem, it is important to note the difference in fluid behavior at the surface. The velocity gradient asymptotically increases as the fluid moves away from the surface. The friction forces of drag reduce the velocity gradient as flow approaches the surface. Moreover, when modeling flow over a flexible surface, the impact of the friction drag force can distort surface geometry and ultimately influence the boundary layer. This proves a high level of significance of determining the skin friction when approaching FSI problems.

2.3 Oil Film Interferometry

Determining accurate measurements of wall shear stress distribution is vital to understanding drag characteristics in aerodynamics. Various techniques to determine wall shear stresses are available, a few examples are summarized here. Preston tubes are inexpensive and convenient for measuring local turbulent skin friction values, however are limited to measuring one location on the surface at a time and are intrusive to flow. More information on Preston tube measurements can be found in [Ackerman and Hoover, 2001]. Another traditional skin friction measurement technique is the Stanton tube. Stanton tubes measure shear stress on the principle that the characteristic height of the tube is small compared to the boundary layer thickness [Trilling and Häkkinen, 1955]. A tube with a pressure orifice on its front face is rested on the surface where the wall shear stress is acting. The pressure from the tube is compared to the local, undisturbed static pressure. These two pressures, along the undisturbed velocity, are a function of the velocity field near the wall. These parameters form a similarity relationship

and are used to calculate local skin friction. Stanton tubes are simple and effective, their low cost is another attractive aspect of this measurement system. Aside from the disadvantage of intruding to flow, different types of Stanton tubes range in a wide variety depending on the testing environment. Each tube must be carefully calibrated in order to produce accurate results, and results are obtained at one location at a time. Details of each measurement method are discussed more in [Winter, 1979]. The traditional methods listed are intrusive to flow and require modification to the structure being measured, such as drilling holes into a flat plate for pressure taps. Additionally, detailed calibration is required, and may produce different results depending on the experimental setup regarding flow conditions and pressure gradients [Garrison and Ackman, 1998].

More recently developed measurement systems include Micro-Electro-Mechanical Systems (MEMS) sensor. A MEMS sensor can serve as an indirect method to measure wall shear stress as shown in studies by [Sheplak et al., 2004, Ghouila-Houri et al., 2017]. A MEMS sensor is placed flush with the wall of a wind tunnel test section to measure flow separation and resulting wall shear stress. This works indirectly because the wall of the wind tunnel is rigid. MEMS shear stress flow sensors are able to function in harsh, high-temperature, high-turbulence environments [O'Grady et al., 2009]. Albeit the sensor is miniature, applying a MEMS sensor to a thin, flexible membrane would significantly impact the natural behavior of the membrane. The resting position would be altered and the frequency of the membrane's flutter would be dependent on the mass and position of the sensor.

Measuring skin friction on a thin, flexible membrane requires an indirect method to avoid the undesirable measurement characteristic that is intrusive to flow. Each of the methods listed above would directly effect the position of the thin membrane during the duration of the experiment. To avoid unnecessary flow obstruction, OFI is the selected method to measure skin friction in this study. A brief overview of OFI is presented here. Oil placed on a surface thins as it is subjected to flow as seen in Figure 2.2. The oil thinning is a result of shear stress acting on the oil. Squire [Squire, 1961] recognized that the thickness or height, h, of an oil film is related to the corresponding shear stress, τ. This relationship is derived from a form of the continuity equation for a boundary layer over a flat plate (Equations 2.9,2.10). Coupling the air and oil flow is achieved at the boundary layer of the oil-air interface ($y = h$), where the velocity and shear stress of the air is specified to be the same as that of the oil [Zilliac, 1996]. The motion of the oil is dependent on shear stress, gravity, pressure gradients, surface tension and surface curvature. The governing equation for this relationship, developed by [Squire, 1961] is given as

$$\frac{\partial h}{\partial t} + \frac{\partial}{\partial x}\left[\frac{\tau_x h^2}{2\mu} - \frac{h^3}{3\mu}\left(\frac{\partial p}{\partial x} - \rho g_x\right)\right] + \frac{\partial}{\partial z}\left[\frac{\tau_z h^2}{2\mu} - \frac{h^3}{3\mu}\left(\frac{\partial p}{\partial z} - \rho g_z\right)\right] = 0, \tag{2.16}$$

where the variables are defined by the oil film thickness (h), time (t), μ is the dynamic viscosity of the oil, p is the pressure, and ρ is the oil density. Here, x and z are the spatial variables in the plane of the surface. τ_x and τ_z are the corresponding shear stresses acting on the plane, g_x and g_z is the gravity on the oil surface plane, $x - z$ plane. Assumptions are made regarding the oil flow being two-dimensional, incompressible oil flow. Moreover, the dominant force acting on the oil film is the shear stress. The pressure gradient term can be neglected because the plate is thin and parallel to the flow field, meaning that large pressure gradients and flow separation is minimal. Further discussion on significantly reducing the pressure gradient in this study is discussed in Chapter 3. The g_x and g_z terms are neglected because the only gravity present is acting in the y direction. The pressure is normal to the surface, and the air boundary layer thickness is much greater than the boundary layer thickness of the oil, resulting in negligible surface tension effects [Zilliac, 1996]. Thus, the pressure gradient, gravity, and surface tension terms can be neglected. This reduces Equation 2.16 to

$$\frac{\partial h}{\partial t} + \frac{\partial}{\partial x}\left(\frac{\tau_x h^2}{2\mu}\right) + \frac{\partial}{\partial z}\left(\frac{\tau_z h^2}{2\mu}\right) = 0. \tag{2.17}$$

The x direction is aligned with the direction of surface tension, which acts in the direction of the uniform flow [Zilliac, 1996]. This reduces Equation 2.17 to

$$\frac{\partial h}{\partial t} = -\frac{\tau_w}{2\mu}\frac{\partial h^2}{\partial x}. \tag{2.18}$$

To find a linearized solution for the differential equation, Equation 2.18, τ_w is assumed constant at $t = 0$, $h = \infty$ and is given by

$$\tau = \frac{\mu x}{ht}. \tag{2.19}$$

However, it is necessary to evaluate τ_w at spatially varying locations when performing OFI, requiring an iterative solution that is shown by 2.21.

The following equations relate to values derived from performing an OFI experiment. An overview of the oil film interferometry process is discussed here. For more information on the oil film interferometry process, see [Tanner and Blows, 1976, Naughton and Hind, 2013, Garrison and Ackman, 1998, Zilliac, 1996]. Equation 2.18 shows that oil-film thickness, h, is necessary in determining the shear stress acting at the surface. Oil is placed on a model's surface and is subjected to a flow condition parallel, or dominantly parallel in curved-geometry cases, to the oil surface as shown in Figure 2.2.

Once the flow is applied, the oil thins along the surface over a period of time. The thinning of the oil is caused by the local shear stress, τ, of the air and oil interaction. A diffused light source is positioned

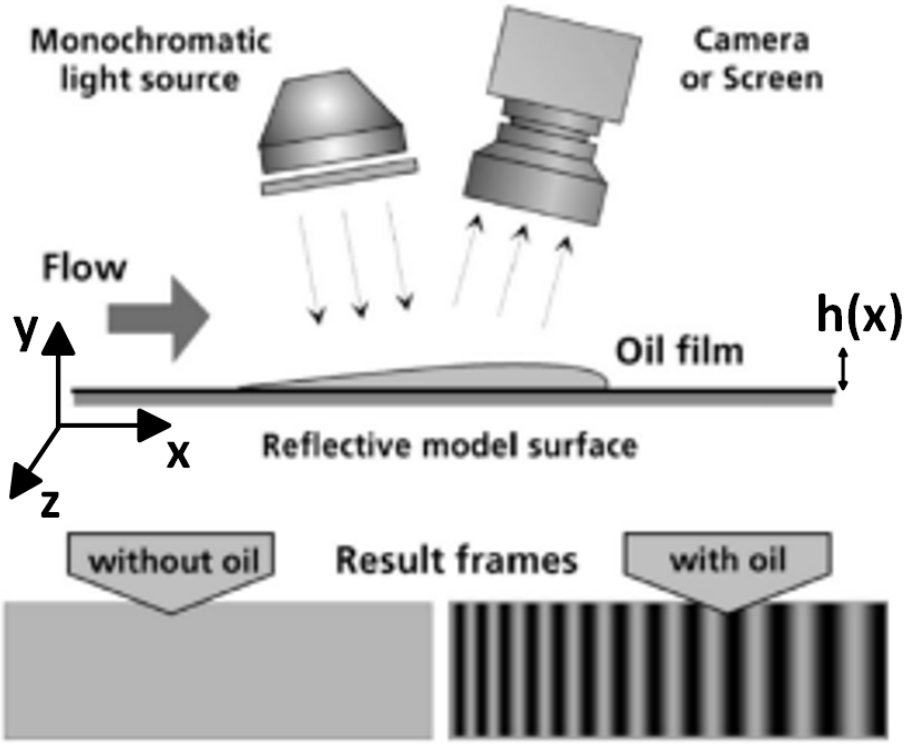

Figure 2.2: Oil film interferometry schematic. From [Lunte et al., 2018].

over the oil surface. The beams of light will reflect in one of two ways: reflect off the surface of the oil, or pass through the oil and reflect off of the surface of the model. These different behaviors cause constructive and destructive interference patterns that is dependent on oil thickness, h, shown in Figure 2.3. The destructive patterns are captured by a CCD camera and recorded to an external storage device for further analysis. The destructive interference band spacing at that instance is directly related to the oil thickness by

$$h = \frac{\phi\lambda}{4\pi} \frac{1}{\sqrt{\left(n_{oil}^2 - n_{air}^2 \sin^2\left(\theta_i\right)\right)}}, \tag{2.20}$$

where the variables are defined as the phase difference (ϕ), illumination wavelength (λ), n_{oil} and n_{air} are the index of refraction for the oil and air, respectively, and incidence angle of light (θ_i)

A modification of Equation 2.18 was developed by [Garrison and Ackman, 1998] is used to iteratively solve for the shear stress as the position of oil changes over time, and is given by

$$\left(\tau_{i+1}\right)^{\frac{1}{2}} = \frac{\int_0^x \left[\frac{n}{\tau_i}\right]^{\frac{1}{2}} dx}{h\sqrt{(n)}\int_0^t \frac{dt}{\mu}}, \tag{2.21}$$

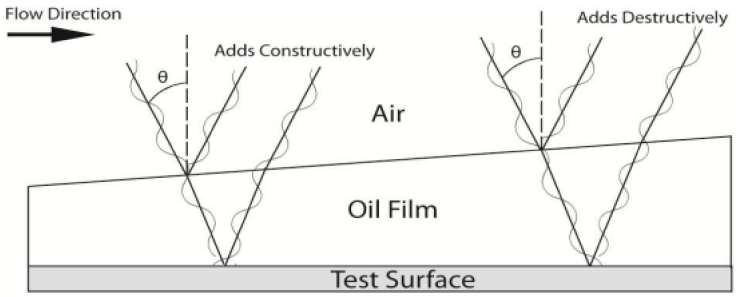

Figure 2.3: Constructive and destructive light interference patterns. From [White, 2011].

where τ_{i+1} is the updated value of the shear stress, τ_i is the previous shear stress value, the local streamline divergence (n), and x is the distance measured from the leading edge of the oil. The iterative solution for the skin friction coefficient C_f can be derived by dividing Equation 2.21 by the dynamic pressure (q), which yields

$$(C_{f,i+1})^{\frac{1}{2}} = \frac{\int_0^x \left[\frac{n}{C_{f,i}}\right]^{\frac{1}{2}} dx}{h\sqrt{(n)}\int_0^t \frac{q}{\mu} dt}, \tag{2.22}$$

where C_f is the skin friction coefficient and q is the dynamic pressure of the fluid flowing over the surface. Because Equation 2.22 is an iterative solution, an initial guess for C_f is needed. [Garrison and Ackman, 1998] suggests that for an approximation of C_f, the shear stress is assumed constant, yielding

$$C_{f,1} = \frac{\mu x}{qht}. \tag{2.23}$$

Oil film interferometry is a simple yet effective experimental technique that does not require extensive calibration. Albeit calibration is necessary for the camera depending on the severity of the lens angle relative to the oil surface. Due to the nature of wall shear stress' dependency on viscosity, calibration of the oil's dynamic viscosity is needed. The development of analysis programs and low-cost image acquisition systems have resulted in many variations of oil film interferometry techniques. The laser interferometer skin-friction (LSIF) meter provides point-wise data for low-speed flows [Tanner and Blows, 1976]. The global interferometer skin-friction (GSIF) meter invented by researchers at NASA Ames Research Center, and further improved upon by [Garrison and Ackman, 1998]. The GSIF meter measures shear data over a broad range of flows that provides more accurate data over larger surfaces at a low cost. A more recent technique developed by [Naughton et al., 2001], and displayed in [Decker, 2002] uses the Windowed

Fourier Transform (WFT) of an oil fringe pattern. This is the measurement technique used in this study's approach and is further expanded on in chapter 4.

2.4 Photogrammetry

An overview of the application of photogrammetry is discussed here, largely covering two important topics relating to this study. [Mikhail et al., 2001, Naughton and Liu, 2007] present more involved principles and other photogrammetry applications that are not directly stated in this section. More details of the implementation of photogrammetry used in this study can be found in Chapter 4.

Photogrammetry calculates the relationship between three-dimensional coordinates of an object and the corresponding two-dimensional image. The applications of photogrammetry are nearly infinite. It is heavily relied on in astronomy, topographic satellite mapping, and geometric design of highways to prevent or significantly reduce image distortion of a two or three dimensional map [Mikhail et al., 2001]. One case of photogrammetry used in this study was to account for image distortion. Image distortion occurs when the plane of the camera lens is not parallel to the plane of the object being captured, or the object itself has multiple planes that need captured. The severity of image distortion primarily relies on the distance from the lens to the object being captured and the angle between the lens and object. A longer distance and larger angle from the plane of interest results in higher distortion of the image. Distortion can be broken up into radial and tangential distortion. Radial distortion is when a straight line appears bent into a curved line, most common in fish-eye lenses or when the object plane is not flat. Tangential distortion, also called de-centering distortion, occurs when the lens is not centered over the image plane. The output of an image appears stretched, compressed, or tilted at an angle as a result of tangential distortion.

The second case of photogrammetry used in this study is more specific to oil film interferometry. The incident light angle, θ_i in equation 2.20 is defined as the angle between the normal of the surface plane and the line where the light hits the surface. In the case of oil film interferometry, this holds true if and only if the camera lens is parallel to the oil surface. Unfortunately, the flat plate experiment is the only direct application where the lens and light source may be parallel, in some cases the camera may need to be angled depending on the setup. Oil film interferometry performed on a curved or angled surface has become increasingly more common due to the simplicity of camera calibration and photogrammetry programs. In the case of this study, a flexible membrane is used as the surface where the oil is placed. Another example being the ramp model studied by [Decker, 2002]. A typical oil film-interferometry system is shown in Figure 2.2. The camera and light source are angled in such a way that produces the most evenly illuminated surface on the image acquisition system. Therefore, θ_i is dependent on both the

orientation of the light source and camera relative to the surface where oil is applied, shown in 2.3. The calculation of this angle is crucial to avoid error in the resulting skin friction value that is derived from the image. Manual distance and angle calculations can be tedious and lead to even more error in the final result. Fortunately, a study by [Naughton and Liu, 2007] shows that the camera angle relative to the oil surface can be eliminated with the application of photogrammetry, reducing skin friction coefficient errors of up to 14%, depending on the distance and angle between the camera lens and surface. Figure 2.4 shows a simple translation between world 3-D coordinates (X, Y, Z) to image mapped 2-D coordinates (x, y).

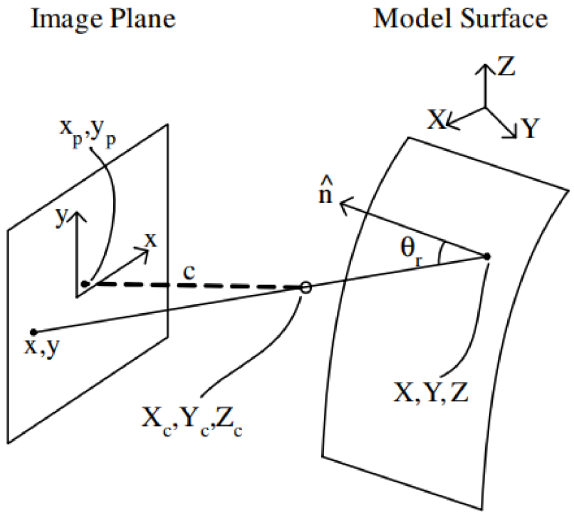

Figure 2.4: World coordinates mapping to an image plane as a result of photogrammetry. From [Naughton and Liu, 2007].

The lens of the camera is modeled by a single point known as the perspective center. The subscript c denotes the perspective center in the object space. The perspective center of the camera relates to the image coordinate system and is defined by interior orientation parameters of the camera including the principle distance (c) and the photogrammetric principle point locations (x_p, y_p). The angle normal of the model surface relative to the camera is denoted as θ_r, and in essence, is the parameter that is eliminated from calculation when photogrammetry. This is because the camera "reorients" itself to be directly normal to the model surface, resulting in $\theta_r = 0\,\text{deg}$. More on the approach to the application of phtogrammetry is discussed in Chapter 4.

2.5 Fluid Structure Interaction

Fluid structure interaction is a broad, complex subject with seemingly unlimited topics to study. For example, a flag fluttering in the wind is a natural, random behavior that can be modeled from various points of view. Both experimental and numerical approaches to FSI problems are abundant in literature. Numerical evaluations may be preferred due to general complications that follow an experimental approach. A few of these complications include equipment cost, limited availability of facilities, along with potential error in calibration, data collection, and analysis. On the other hand, the fact that FSI occurs in nature limits the accuracy of a numerical approach because of pre-defined assumptions and conditions that are required when modeling a numerical approach. A focal point in studying FSI, particularly cases where the structure is flexible, is the instability in the transition region between a laminar to turbulent boundary layer. [Benjamin, 1960] presents the possibility of nearly eliminating or delaying the transition region by applying a flexible skin to a rigid body. While this is a favorable result, new instabilities may arise due to the nature of a non-rigid structure, making the flexible skin useless if not carefully analyzed. Further studies by [Gyorgyfalvy, 1967] extensively models the possibilities of reducing skin friction drag over a body by applying a flexible skin. Thollmein-Shlichting waves are an instability of small disturbances that are developed in the laminar regime of the boundary layer, leading to the occurrence of transition to turbulent flow. Amplification of Thollmein-Shlichting waves are compared with instability limits of the boundary layer. Conclusions state that ultimately a flexible skin delays boundary layer transitions, and the main effect of the skin is on the amplification of the Thollmein-Shlichting waves rather than the instability limits. However, the study was a numerical simulation and the characteristics flexible surface had to be selected in such a way to produce a favorable result.

This leaves a void in expanding experimental wall shear stress measurements to a wider range of applications. Natural occurrences of FSI on a flexible body are random without specified characteristics. A controlled experimental approach is necessary to better analyze and understand these random and natural behaviors.

Chapter 3: Experimental Setup and Instrumentation

3.1 Overview

To validate the design of the skin friction measurement system, two flow facilities were used. The Experimental Fluids and Aerodynamics Lab (EFAL) at the University of Idaho has a laminar jet and a research-grade wind-tunnel. Prior to performing OFI measurements, hot wire anemometry was used to quantify a velocity profile in the wind-tunnel's test section. OFI was then performed on a flat plate model to validate the OFI system before conducting the experiment in the jet facility on the thin, flexible membrane model. The following chapter discusses details about the setups, instrumentation and facilities used.

3.2 Wind Tunnel Facility

The wind tunnel located in the Experimental Fluids and Aerodynamics Lab at The University of Idaho was used in conducting both HWA and OFI experiments. It is an open-circuit, Eiffel type wind tunnel with an airspeed range of 0-70 $\frac{m}{s}$ (1-160mph) shown in Figure 3.1. It is 11.278m (37ft) in length and has a 37kW AC induction motor that drives a 1.22m (48in) axial fan. The rectangular test section is 0.457m x 0.457m x 0.914m (18in x 18in x 36in) made of 19.05mm (0.75in) thick Plexiglas, providing optical access. It consists of a removable top pane, bottom pane, and two circular access ports with a diameter of 15.24cm (6in). A honeycomb layer and 3 mesh screens at the intake of the wind tunnel provide a uniform flow in the test section, decreasing turbulence intensity by up to 0.5%. The contraction ratio of 3.8 between the inlet and test section reduces span-wise velocity and accelerates flow towards the test section. The user operates the wind tunnel using a variable frequency controller. A Dwyer Durablock manometer (shown in Figure 3.9) is connected to the wind tunnel, providing dynamic pressure readings within the test section. For more details on this wind tunnel, see [Cunnington et al., 2002].

3.3 Laminar Jet Facility

The Experimental Fluids and Aerodynamics Lab has a subsonic, laminar jet facility with a vertical flow output, shown in Figure 3.2. Flow is driven by an electro-craft motor connected to a centrifugal fan, and air flow is controlled by varying RPM, shown in Figure 3.10. The jet's nozzle provides a smooth flow transition between the immediate outlet and stilling chamber. Flow inside the jet's stilling chamber

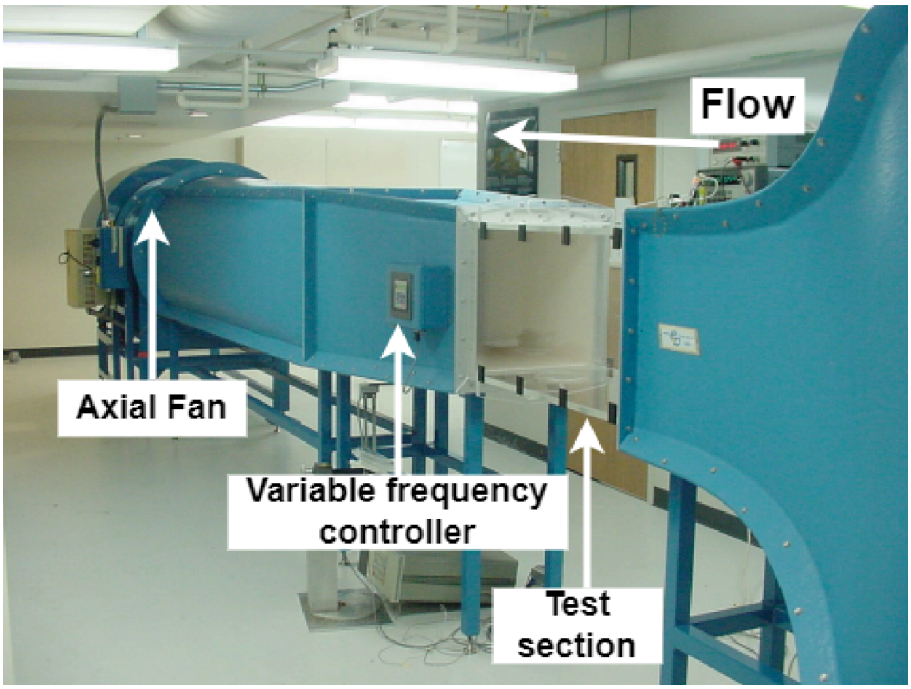

Figure 3.1: Wind tunnel located at University of Idaho's EFAL.

is conditioned by three sets of fine mesh and a 22.86cm (9in) long honeycomb layer. The jet free-stream velocity (U_∞) ranges from 0 to 24$\frac{m}{s}$.

3.4 Flat Plate Model

In order to perform OFI on over a flat plate in the wind tunnel, a 3-D printed support was modeled around an existing mirror polished, stainless steel rectangular plate. The plate was 127mm x 127mm (5in x 5in), with a nominal thickness of 2.705mm (0.1065in). The objective of the 3-D printed model was to negate large pressure gradients and flow separation over the plate. A leading edge in the shape of a cubic super-ellipse with an axis ratio of 6 would avoid such flow separation over the plate [Narasimha and Prasad, 1994]. This model consists of continuous curvature which greatly reduces the severity of the pressure gradient. The curve is given by the following relationship

$$[(a-x)/a]^n + (y/b)^n = 1, \tag{3.1}$$

where a is the length of the nose, x is the horizontal distance along the plate, n is an elliptical index where $n > 2$, y is a constant thickness from the center, and $2b$ is the thickness of the rectangular model in this case. To obtain the coordinates for the curve of the super-ellipse, Equation 3.1 is modified to

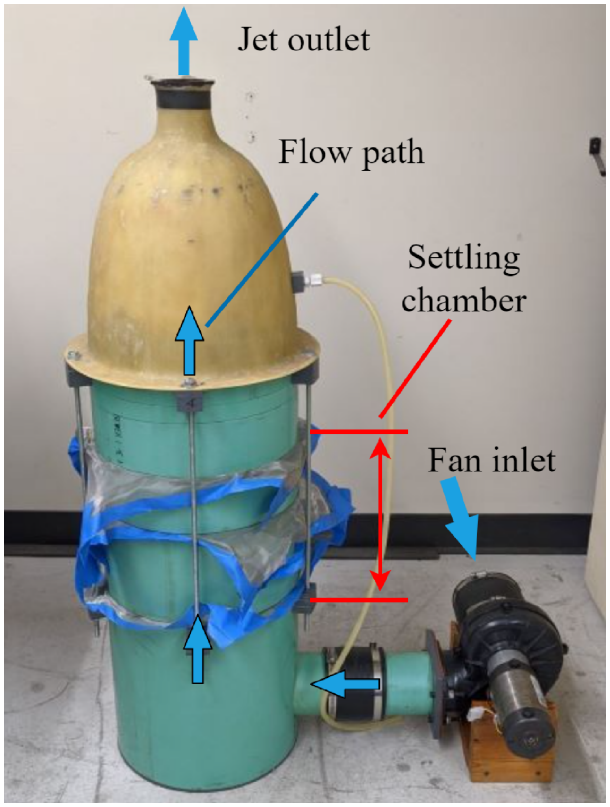

Figure 3.2: Jet facility located at University of Idaho's EFAL.

solve for y and plotted against x as shown in Figure 3.3a. To ensure continuous curvature when being 3-D printed, 3000 data points were plotted. The coordinates were uploaded into a SolidWorks curve to create the leading edge of the flat plate support, shown in 3.3b, and the rest of the design was modeled about the existing flat plate, shown in Figure 3.4.

The plate was measured with a micrometer to ensure uncertainties in the press-fit indentation, where the plate rests, were negligible. Five 1.59mm (0.0625in) thru-holes were present in the base of the model for easy detachment of the steel plate for cleaning and disassembling purposes. The model was printed from a Stratasys J850 Pro 3-D Printer using VeroUltra resin with a resolution of 14 microns.

3.5 Flexible Membrane Model

A thin, flexible membrane, or flag, was used as the surface that the oil was placed on, as shown in Figure 3.5. The membrane has a thickness of 0.127mm (0.005in), a width of 19.05mm (0.75in), and a height of 88.9mm (3.5in). The membrane was a stencil cut-out from a laser cut model of wood. The membrane was pulled in tension and supported by a custom stand that attached to an ATI Mini-40 SI-20-1 force and torque transducer load cell. The load cell actively collected aerodynamic force data

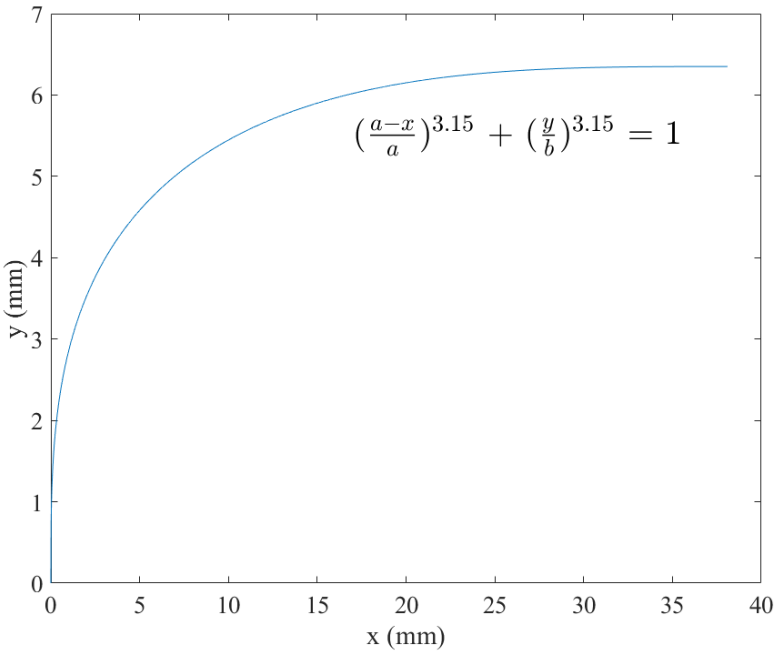

(a) Leading edge cubic super-ellipse curve

(b) Resulting leading edge applied to the 3-D printed model

Figure 3.3: (a)Leading edge coordinates and (b) applying the curve to a solid model

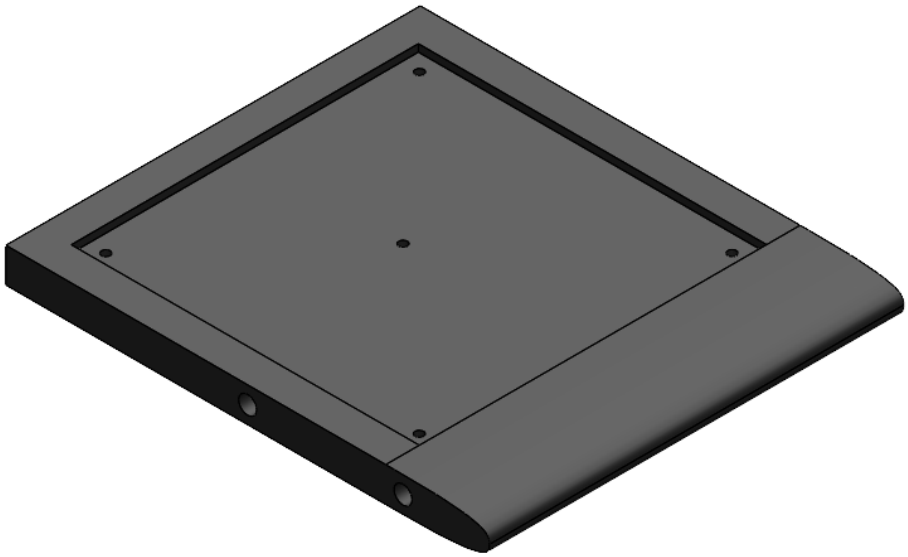

Figure 3.4: 3-D printed model to prevent flow separation at the leading edge of the flat plate.

that was modeled as the total drag force acting on the flag. The diameter of the stand, D_1=117.5mm, is twice the diameter of the jet nozzle, D_2=63.5mm, to ensure the mounting mechanism was not influenced by the fluid flow that exits the jet nozzle. Also included in the mounting design is a rotating mechanism that allows for change in angle of attack relative to the flow direction.

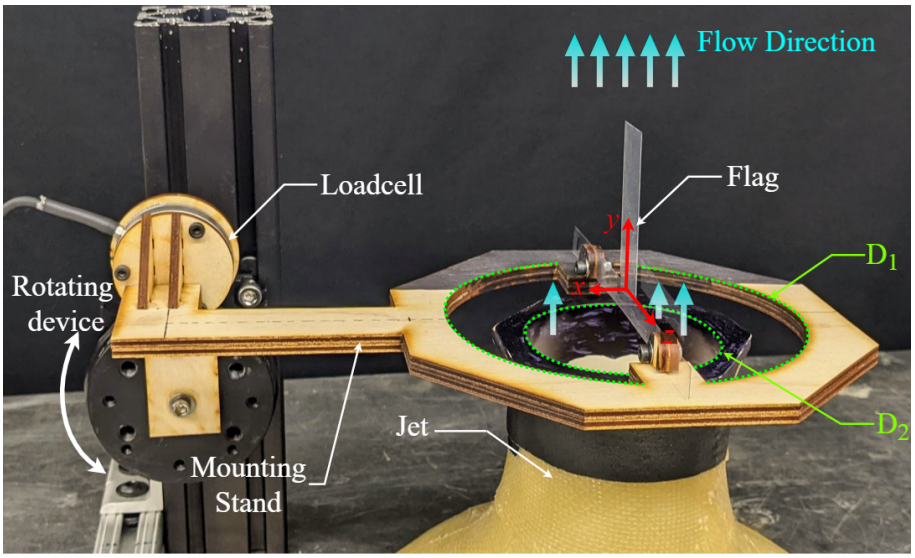

Figure 3.5: Flexible membrane, mounting mechanism and load cell.

3.6 Hot Wire Anemometry

Hot wire anemometry was performed to profile the test section of the wind tunnel. The constant temperature anemometer used was a TSI-Intelligent Flow Analyzer-100 (IFA-100). The probe used was a TSI-model 1260A miniature (1.5mm) straight probe with an operating temperature of 250°C shown in Figure 3.6. The probe support was fed through an existing hole in the access port of the test section. The primary output signal was connected to a NI-Instruments Data Acquisition System (NI-DAQ) where voltage readings were displayed using LabView. This output signal was also teed to a Khron-Hite Bessel function low-pass filter to avoid aliasing. The secondary output jack was connected to a Tektronix Oscilloscope to optimize the output signal to match the manufacturers square wave during calibration. Measurements were taken at various locations using a vertical traverse mechanism. A custom stand was built to support the traverse mechanism, shown in Figure 3.7. The resolution of the traverse mechanism is 0.001in. The BNC cable attached to the IFA-100 was 6m long to reduce the effects of cable resistance during data collection. A 3-D printed clamp was designed to secure the probe support to the traverse mechanism and prevent oscillation within the test section.

Velocities measured ranged from 15-50m/s at three distinct heights from the base of the test section.

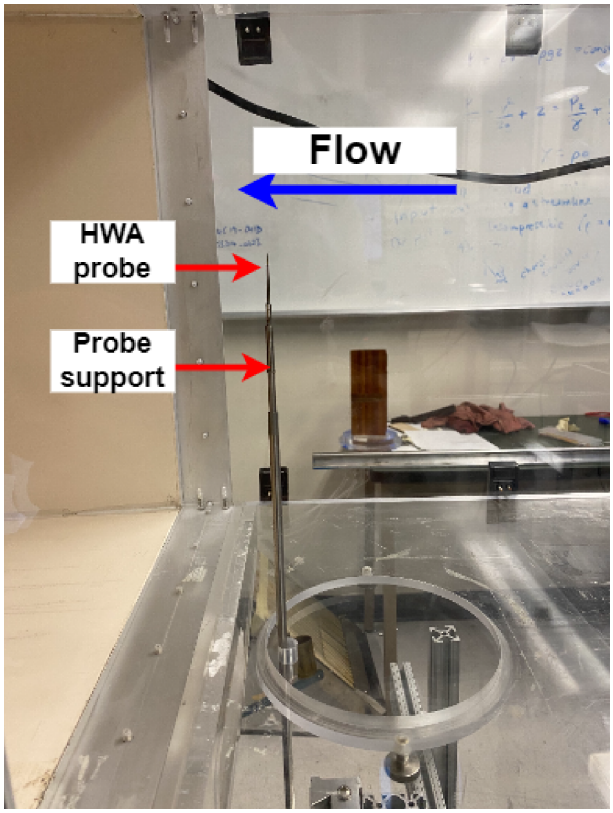

Figure 3.6: Probe and probe support inside test section.

Data was collected at 6kHz for 300 seconds. The low-pass filter was set to a cutoff frequency of 3kHz, which is the resulting Nyquist Frequency of the system, to avoid aliasing. This leads to a total of 1,800,000 data points recorded for each velocity.

3.7 OFI

The test section of the wind tunnel can be accessed by removing either the top or bottom pane of Plexiglas. Therefore, the OFI assembly was designed around this restriction. Figure 3.8 shows the assembly and components that are within the test section during testing. The 3-D printed model is sandwiched between two 5.59mm (0.22in) thick panels of acrylic. The leading edge of the 3-D printed model was centered 30.4cm (1ft) downstream of the leading edge of panels to avoid any flow separation that may occur on the upstream edge of the panels. Two all-thread rods were fed through the side of the model and connected to the laser cut panels to raise the 3-D printed model from the base of the wind tunnel test section, and secure the 3-D printed model to the acrylic panels. Rubber stops were epoxied to the top corners of the acrylic to secure and stabilize the assembly in the test section. When the top panel of the test section is reattached for testing, there is a downward force on the rubber stops to prevent

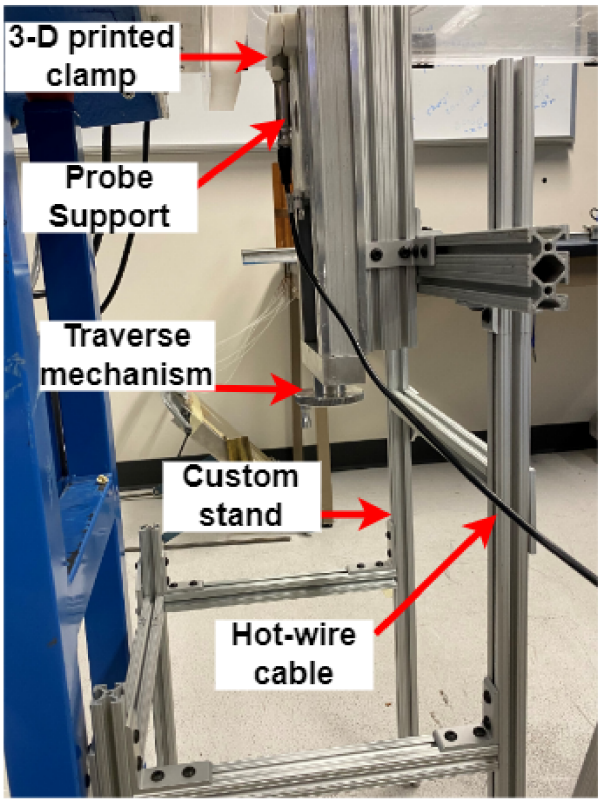

Figure 3.7: HWA stand, probe support, 3-D printed clamping mechanism, and sliding traverse mechanism.

movement.

Image data was acquired using a Basler Ace 2 camera (model a2A1920-51gcPRO) attached to a 50mm Nikon lens and a 532nm band-pass filter. The wind-tunnel OFI setup is shown in Figure 3.9, and he jet OFI setup is shown in Figure 3.11. The images were processed using NI max and LabVIEW software, where an acquisition code was written. The user has the ability to change critical camera parameters including exposure, frame rate, gamma value, etc., to optimize the image output. Frame rates were adjusted based on the speed of the flow for a particular run. For example, the oil fringes form much slower at a lower velocity, therefore it was not necessary to acquire images at a high rate. An LED light source was used with attached layers of diffuser-paper to provide a more evenly illuminated output image. The light source was centered over the oil surface in both the wind tunnel and jet OFI setups.

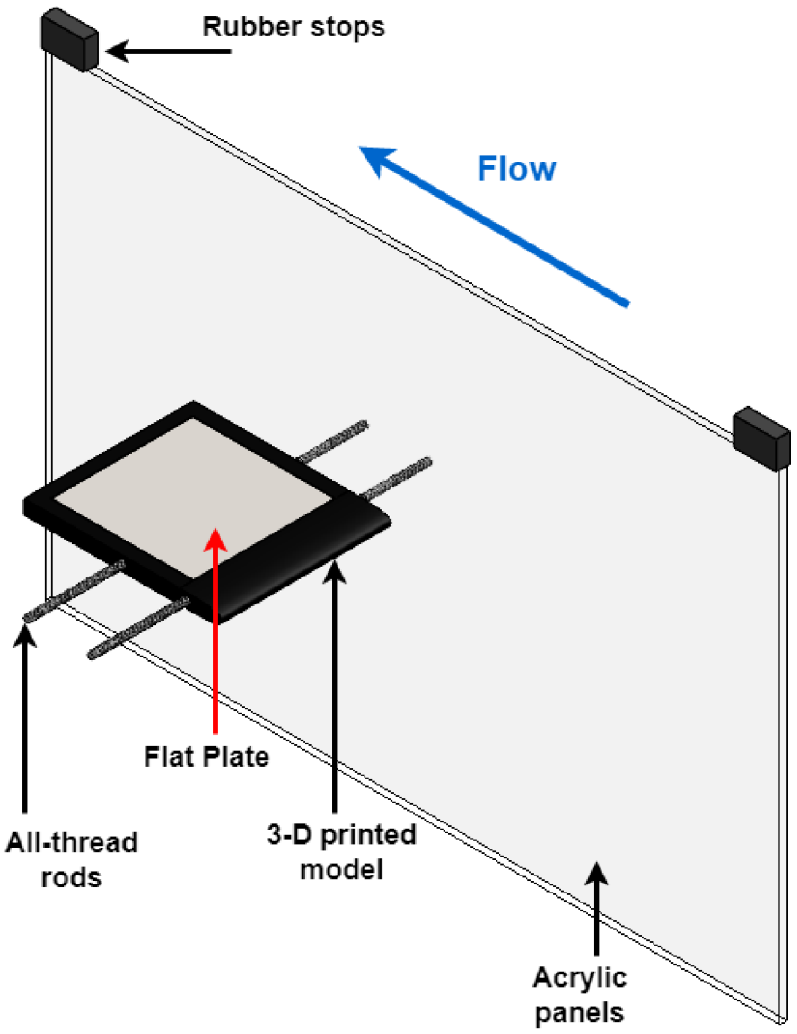

Figure 3.8: Oil film interferometry setup for the wind tunnel. Note: one acrylic panel is removed here to show detail of setup.

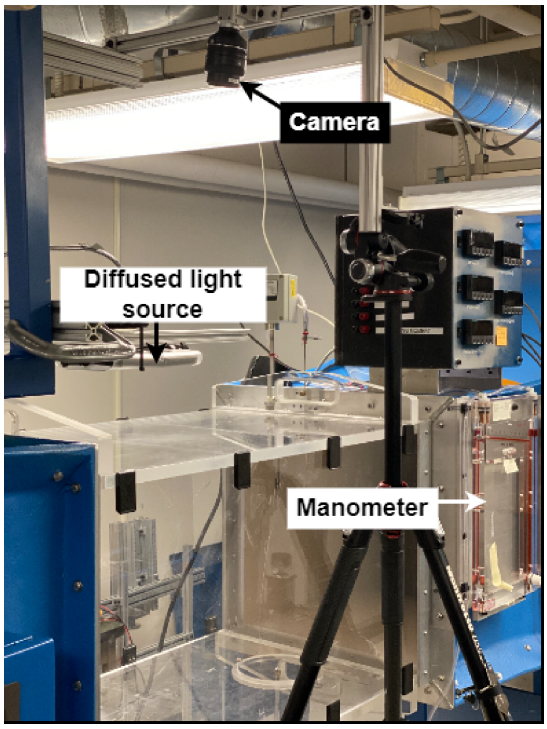

Figure 3.9: Wind tunnel OFI setup.

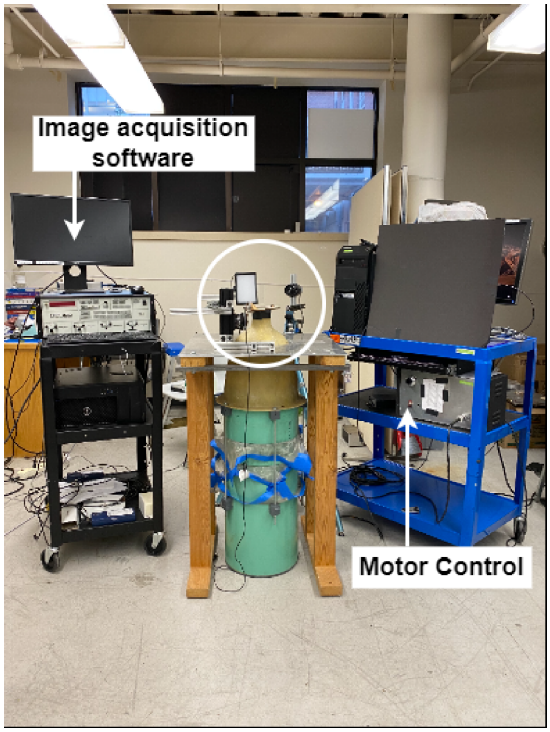

Figure 3.10: Jet OFI setup. The circled area is shown with greater detail in Figure 3.11.

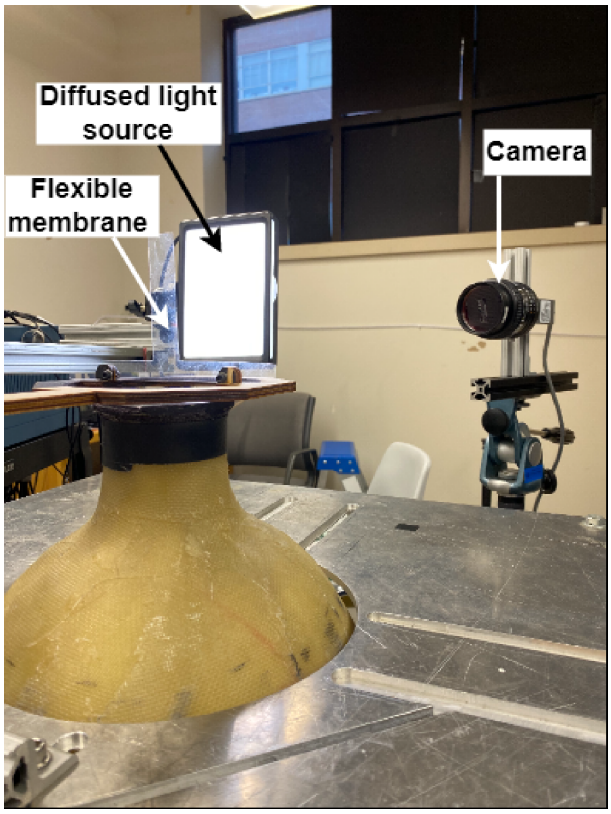

Figure 3.11: OFI setup showing the light source, flexible membrane, and camera detail.

Chapter 4: Approach

4.1 Image Correction

Photogrammetry was applied using the camera calibration function in MATLAB R2021b. The function calculates errors and provides an undistorted image output from an image that is subject to distortion. The function requires a calibration image with a pattern with known dimensions. For this study, a checkerboard was used, where the distance between black and white squares are 1mm. These known dimensions are referred to as world coordinates because the dimensions are independent of the image being taken. The program re-projects corners of the checkerboard where the black and white squares intersect as translation and rotation matrices, as shown in Figure 4.1.

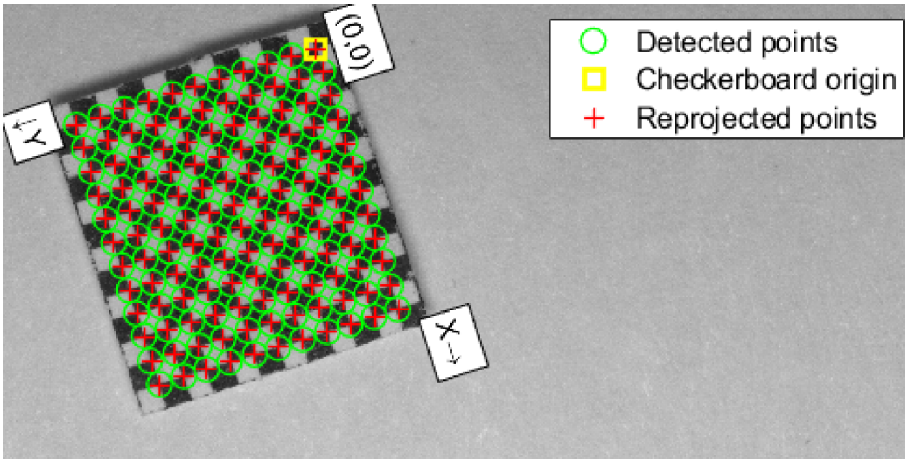

Figure 4.1: MATLAB Calibration Application detecting and re-projecting corners of the checkerboard based on the image distortion matrix

A brief overview of the image correction algorithm is given below. For more information on the camera calibration application, see [MATLAB, 2021]. The algorithm is used to relate world coordinates to image coordinates and for a standard camera, (i.e. not a fish-eye lens) is given by

$$w \begin{bmatrix} x & y & z \end{bmatrix} = \begin{bmatrix} X & Y & Z & 1 \end{bmatrix} \begin{bmatrix} R \\ t \end{bmatrix} K, \tag{4.1}$$

where (X, Y, Z) are the world coordinates of a point, (x, y, z) are the image coordinates of the corresponding image point in pixels, w is an arbitrary homogeneous coordinate scale factor, R is the matrix representing the 3-D rotation of the camera, and t is the translation of the camera relative to the world

coordinate system. The camera intrinsic matrix (K) in Equation 4.1 is defined as

$$K = \begin{bmatrix} f_x & 0 & 0 \\ s & f_y & 0 \\ c_x & c_y & 1 \end{bmatrix}, \tag{4.2}$$

where (c_x, c_y) represent the principle point in pixels, and s is the skew parameter. Furthermore, f_x and f_y are expressed in pixels and are a function of the focal length (F), in world units and are given by

$$f_x = F * s_x; \quad f_y = F * s_y, \tag{4.3}$$

where s_x and s_x are the number of pixels per world unit in the x and y respectively. The rotation matrix (R) and translation matrix t are then applied to the original image.

After the images are undistorted, the pixel distance must be converted to world units. In the flat plate OFI experiment, cross reference markings were printed with a known center-to-center distance of 6 millimeters, shown in Figure 4.2.

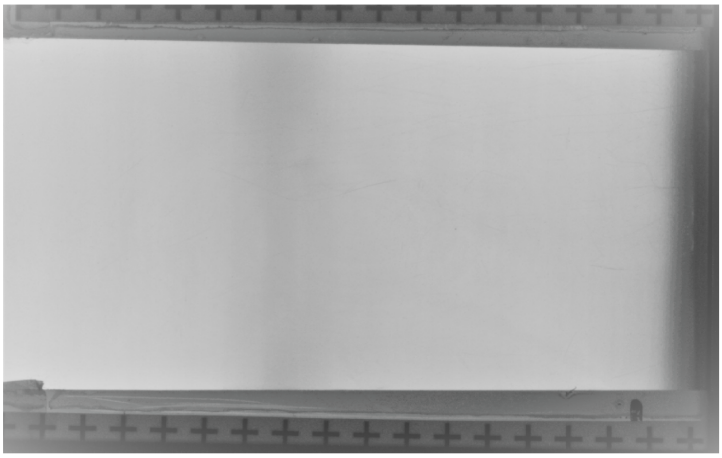

Figure 4.2: Reference markings used for flat plate experiment. Note a filter was applied to original image to improve visibility of markings.

By selecting the center pixel locations of two cross-markings, the difference in pixels is converted to millimeters based on the known distance. The flexible membrane OFI experiment presented somewhat of a challenge in placing reference markings for the necessary pixel-to-millimeter conversion. Due to the flexible nature of the membrane, any reasonable load acting on its surface significantly effects its behavior in fluid flow. Therefore, paper printed markings were not used. Printing markings on transparent film was considered. However, the standard printing process applies heat and bending to the film, leaving

the resulting marked film not only bent, but also has potential for its material properties to be altered. A small permanent marker was used to create reference markings on the flexible membrane, shown in Figure 4.3.

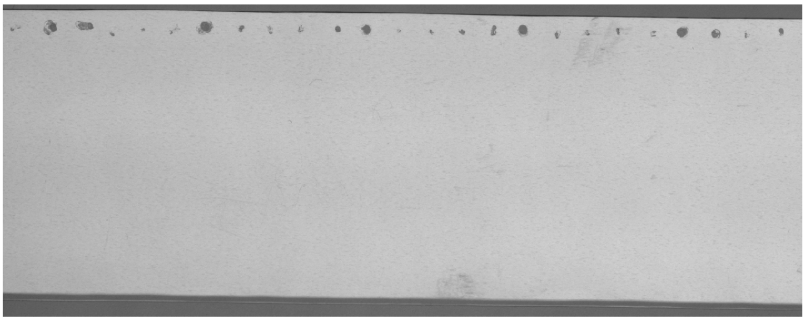

Figure 4.3: Reference markings used for flexible membrane experiment.

Calibration images were acquired at different angles and orientations relative to the camera lens plane. Images were uploaded into the program and calibrated. Images were filtered based on mean pixel re-projection error of the detected points, as shown in Figure 4.4a. Camera intrinsic and extrinsic parameters are estimated in the program and coupled with standard error. Intrinsic estimations include focal length (pixels), principal point (pixels) and radial distortion. Extrinsic estimations include the rotation and translation vectors that re-shape the image matrix. The image coordinates are re-shaped into world coordinates, shown in Figure 4.4b.

After the calibration matrix was determined, an OFI image was uploaded and undistorted based on the calibration matrix. The resulting undistorted output image was then used for further fringe analysis.

4.2 OFI Analysis

To detect oil film fringes and ultimately derive skin friction values in this study, the automated interference fringe pattern recognition method developed by [Decker and Naughton, 2001, Naughton et al., 2001, Decker, 2002] is used. Moreover, the combined approach of several techniques applied by [Decker, 2002] is closely followed in this study and should be referenced for more details and origins of the method. This is a proven analysis technique that results in low random error and is an efficient way to analyze many data points about a single image. An outline with will be given here regarding key equations and analysis steps. The analysis is applied after images are acquired and image distortion is corrected for using photogrammetry. A sample analysis of one intensity line is provided here.

Images are first analyzed by selecting a line along the fringe pattern that detects high and low intensity values, as shown in Figure 4.5. The extracted intensity line is related to pixel distance along the image

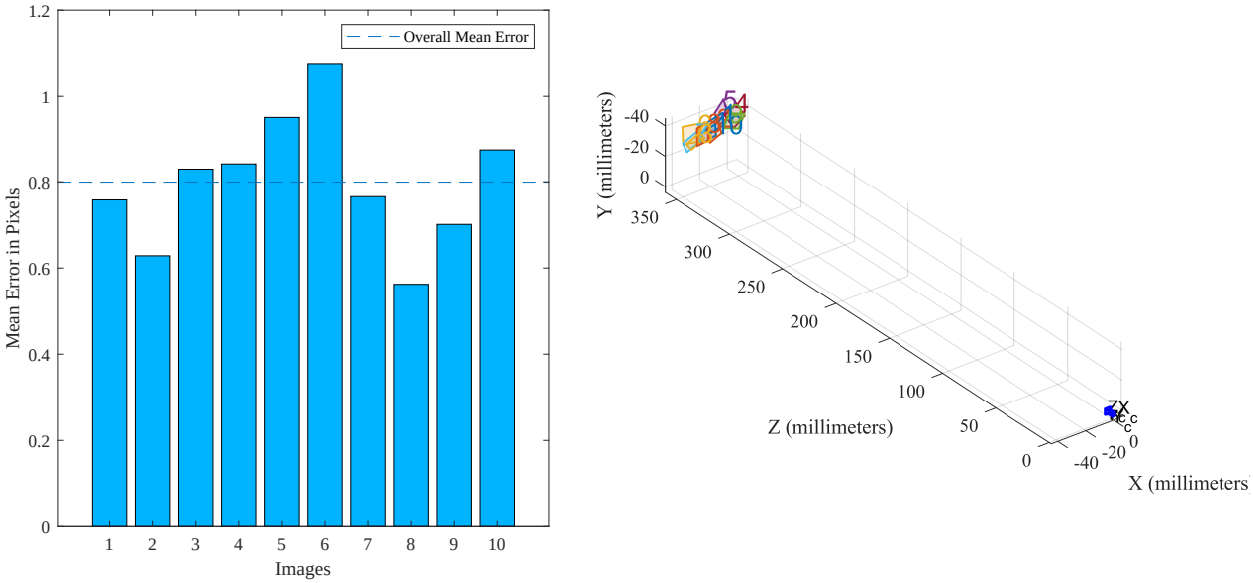

(a) (b)

Figure 4.4: (a) Re-projection error for each image used for calibration and (b) projection of world coordinates of the image positions relative to the camera location

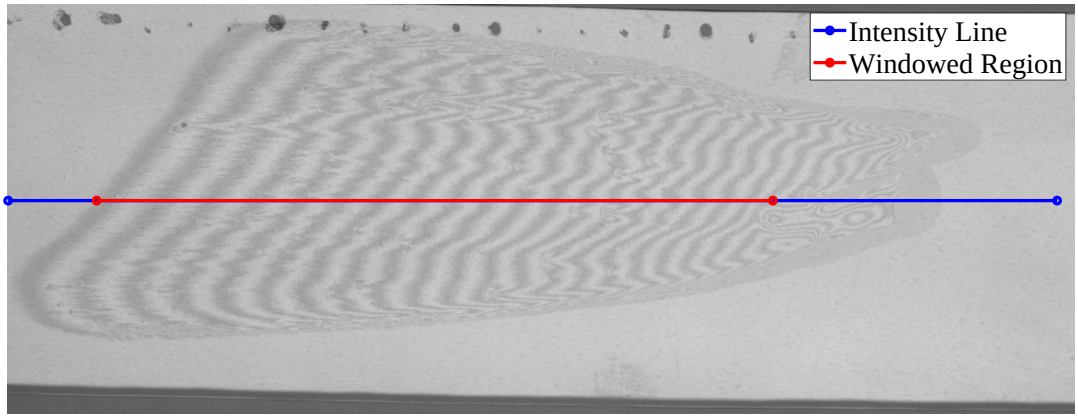

Figure 4.5: Sample image of oil fringe pattern and intensity line.

shown in Figure 4.6a. As seen here, noise is present in the intensity signal, making it difficult to detect the corresponding peaks and valleys. Therefore, an adanced analysis approach is used here. A windowed region of the intensity line is defined to shrink the size of the data set and remove unnecessary data from the intensity signal that are not of interest, shown in Figure 4.6b. Intensity peaks correspond to intensity maxima and valleys correspond to intensity minima. The distance between a peak and valley

corresponds to the distance between a dark and light fringe. Isolating peaks and valleys can provide information about oil height and finally the estimation of wall shear stress and skin friction coefficient values.

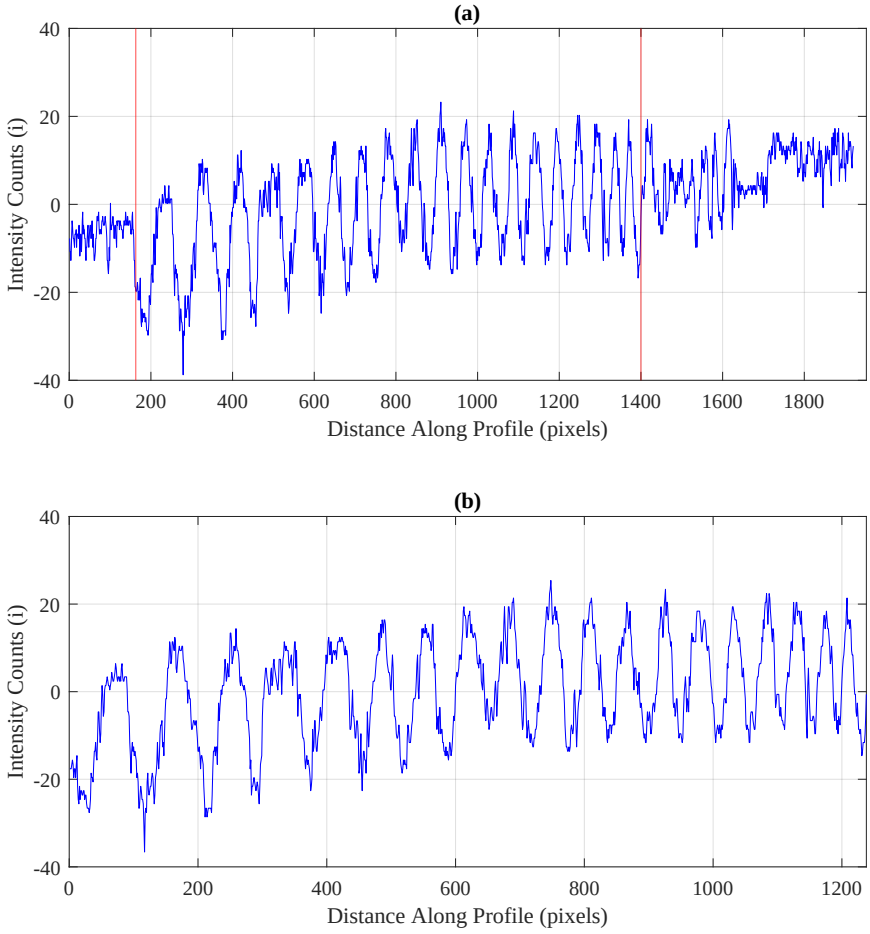

Figure 4.6: (a) Raw intensity signal and (b) windowed region of intensity signal.

It is evident that noise is prevalent in the intensity signal shown in 4.6. To improve the signal quality, the following steps are performed. The Fourier transform of the windowed region is taken, where the point of interest is the maximum amplitude of the intensity signal, $S_{I,I}$, that is a non-zero frequency, shown in Figure 4.7.

A single-period cosine wave shown in Figure 4.8 constructs an interrogation signal using the maximum frequency. A cross correlation between the interrogation signal and signal in the original windowed region is determined and denoted as the auto correlation value ($R_{i,i}$). The cross correlation coefficient ($\rho_{i,if}$) is

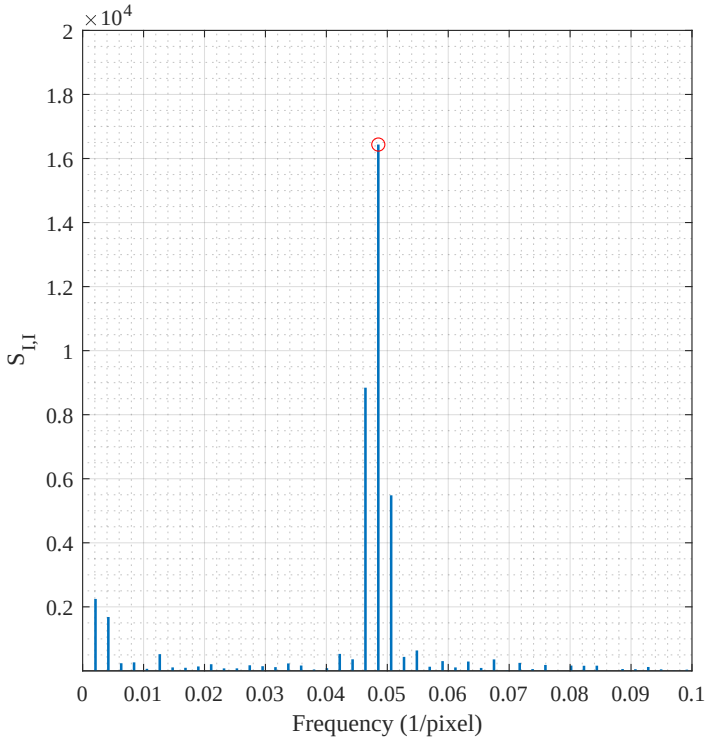

Figure 4.7: Autopectral density of the intensity distribution.

derived by the relationship

$$\rho_{i,if} = \frac{R_{i,if}}{\sqrt{R_{i,i}\left(0\right) R_{if,if}\left(0\right)}}, \tag{4.4}$$

where $R_{i,i}\left(0\right)$ and $R_{if,if}\left(0\right)$ are the auto-correlation values at an offset of zero. Figure 4.9 shows the result of the cross-correlation coefficient applied to the windowed signal.

The noise from the original signal is significantly reduced, and the peaks and valleys are isolated on opposite sides of zero. It should be noted that in some cases of low image quality or poor fringe development, there are peaks and valleys that do not directly correspond to the difference in dark and light fringes. Therefore, the user defined a threshold $\rho_{i,if}$ is determined to further eliminate these undesirable peaks and valleys from further analysis. The improved signal is now used to determine the shear stresses and skin friction coefficient.

The oil thickness at the intensity minima and maxima, or peaks and valleys, are directly related to the local shear stress. Therefore, the phase difference, ϕ, in equation 2.20 can be replaced with the fringe

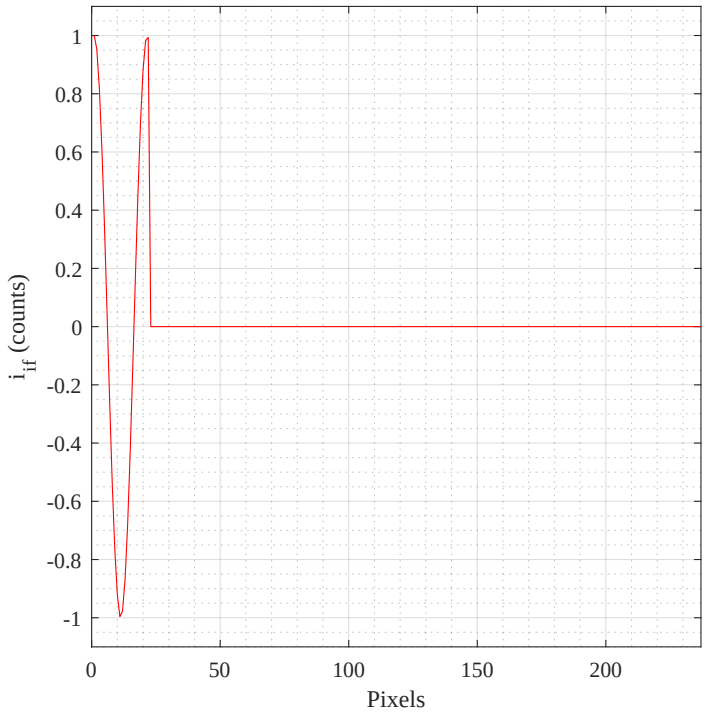

Figure 4.8: Interrogation fringe.

number (k). This modification to the oil thickness is given by

$$h = \frac{k\lambda}{4\pi} \frac{1}{\sqrt{\left(n_{oil}^2 - n_{air}^2 \sin^2\left(\theta_i\right)\right)}}, \tag{4.5}$$

where λ is the illumination wavelength, n_{oil} and n_{air} are the oil and air indicies of refraction, respectively, and θ_i is the incident light angle. The fringe number term, k, is counted as the first peak being 1, the first valley being 2, and so on. Figure 4.10 shows the resulting height.

Once the height is known, the iterative process to estimate C_f begins, and is given by

$$\left(C_{f,i+1}\right)^{\frac{1}{2}} = \frac{\int_0^x \left[\frac{n}{C_{f,i}}\right]^{\frac{1}{2}} dx}{h\sqrt{(n)} \int_0^t \frac{q}{\mu} dt}, \tag{4.6}$$

where the approximate estimate for the initial skin friction value, $C_{f,1}$, as suggested by [Garrison and Ackman, 1998], is given by

$$C_{f,1} = \frac{\mu x}{qht}. \tag{4.7}$$

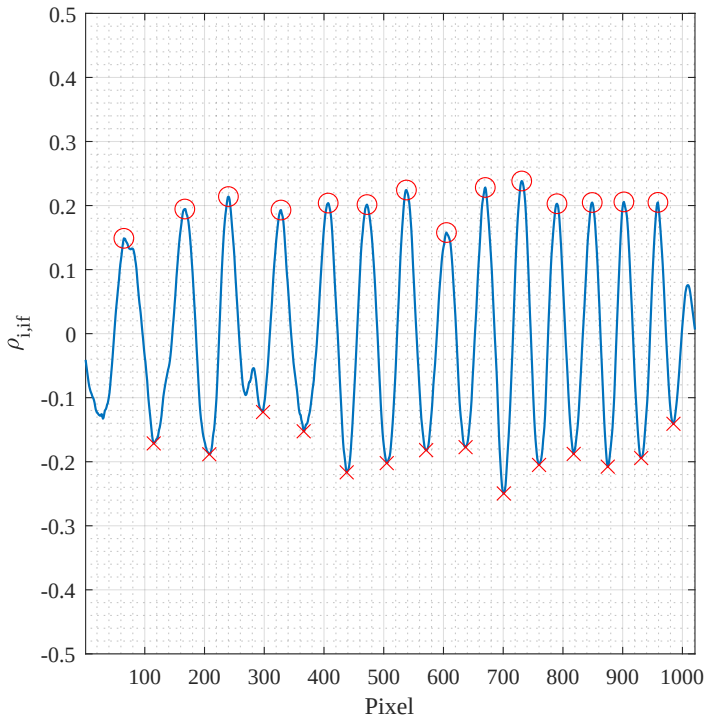

Figure 4.9: Cross correlation coefficient applied to the intensity signal.

The process is followed until a user selected convergence criteria is met. For this study, the convergence criteria was set to 0.0001, at which point a solution for C_f was determined. Several intensity lines can be extracted from a single image to gather many data points about the image. The results of this study shown in Chapter 6 represent the averages of multiple intensity lines along an oil fringe pattern. This approach here can provide a large data set that can be spatially averaged to provide a distribution with a low random error.

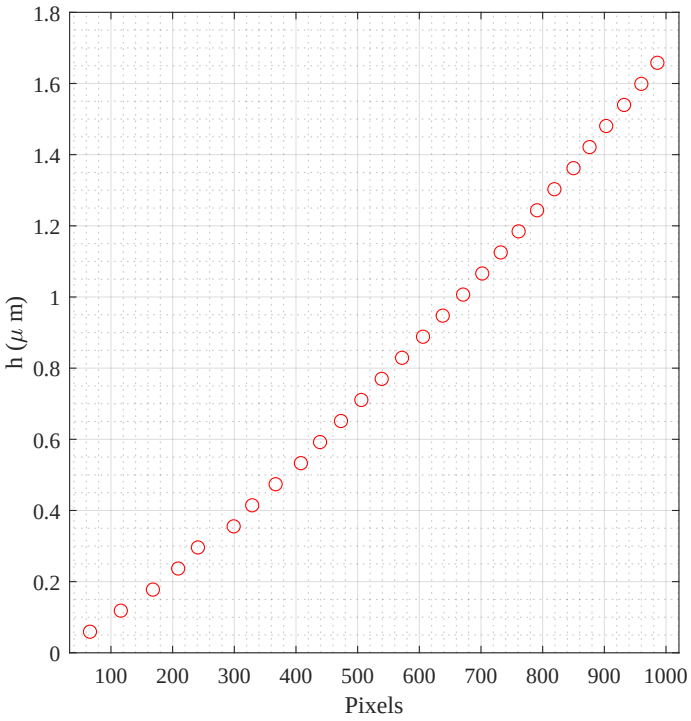

Figure 4.10: Oil film height.

Chapter 5: Uncertainty Analysis

5.1 Overview

A detailed discussion of uncertainty in the key parameters regarding OFI are presented here. First, uncertainty in density is presented. The uncertainty in density plays a role in the dynamic pressure calculation needed for the estimation of the skin friction coefficient. Next, uncertainty in oil viscosity is discussed, and finally a summary of uncertainty in skin friction calculation from OFI is presented.

5.2 Density Uncertainty

Air density, ρ, is calculated by

$$\rho = \frac{P_{atm}}{RT_{atm}}. \tag{5.1}$$

The variable P_{atm} is the atmospheric pressure and has an uncertainty, $U_{P_{atm}}$ of 0.01inHg. The universal gas constant for air, R, is 286.05 J/(kg K) and is assumed to have a negligible uncertainty. The variable T_{atm} is atmospheric temperature and has an uncertainty, $U_{T_{atm}}$ of 0.1 deg C. The total uncertainty in the calculated density is represented by

$$U_\rho^2 = \left(\frac{1}{RT_{atm}}\right)^2 (U_{P_{atm}})^2 + \left(-\frac{P_{atm}}{RT_{atm}^2}\right)^2 (U_{T_{atm}})^2 . \tag{5.2}$$

The uncertainty ratio for density is expressed as

$$\left(\frac{U_\rho}{\rho}\right)^2 = \left(\frac{U_{P_{atm}}}{P_{atm}}\right)^2 + \left(\frac{U_{T_{atm}}}{T_{atm}}\right)^2, \tag{5.3}$$

which results in an uncertainty ratio, $\frac{U_\rho}{\rho}$, of 0.41%.

5.3 Error Propagation

The length and width of the characteristic area of the flexible membrane was measured using a dial caliper with a resolution of 2.54×10^{-5}m. At a 95% confidence level, the uncertainty in width measurements are 0.6%, and uncertainty in length measurements are 0.9%. The manometer used for dynamic pressure readings and velocity calibration in the wind tunnel has a resolution of 0.01inH_2O from 0 to 1inH_2O, and a resolution of 0.1inH_2O from 1 to 10inH_2O.

5.4 Oil Calibration

Oil viscosity calibration is a crucial parameter when performing OFI experiments due to wall shear stress being a function of dynamic viscosity. For this study, Dow Corning PMX-200 oil was used at kinematic viscosities of 10cSt and 50cSt. Equation 5.4 determines oil viscosity at temperatures other than the temperature at which the oil was calibrated at by the manufacturer. The kinematic viscosity calibration expressed in [Zilliac, 1996], and is given by

$$\nu_{o,T} = exp\left[\frac{C_1}{T + C_2} - \frac{C_1}{T_{cal} + C_2} + LOG_{10}\left(\nu_{o,cal}\right)\right] \tag{5.4}$$

where T is in degrees Kelvin, C_1=774.862, and C_2=2.649. $\nu_{o,T}$ is the desired kinematic viscosity at temperature T, and $\nu_{o,cal}$ is the manufacturer's calibrated viscosity at the calibrated temperature T_{cal}. The resulting calibrated viscosity has a typical accuracy of 0.12% of ν per °F of the temperature difference $(T - T_{cal})$, in addition to the $\nu_{o,cal}$ uncertainty. This is critical for determining the oils calibrated dynamic viscosity, μ.

5.5 OFI Uncertainty

The uncertainty parameters in Table 5.1 are derived by [Zilliac, 1996], and are error sources for all OFI measurements that use a similar variation of the experimental setup and instrumentation used in this study. Zilliac improved the Fringe Imaging Skin Friction Technique (FSIF) by utilizing a PC-based application to obtain high resolution skin friction measurements, and quantifying error analysis in the OFI procedure. The parameters in this study are significantly comparable to the parameters discussed in [Zilliac, 1996]. Thus, relating uncertainty evaluations is necessary.

Table 5.1: OFI error sources

Error source	**Uncertainty range**	**Remarks**
Initial oil condition	-0.3% to -0.2% of C_f	Dependent on μ_o and t. Always a negative contribution to total error.
Oil viscosity	± 0.2% to ± 5% of ν_o	Manufacturer's ν_o specification is ± 5%.
Light source wavelength	0% to ± 0.7%	Theoretical uncertainty for white light LED.
Oil index of refraction	± 0.015% of n	n is slightly temperature dependent. A refractometer should be used in future studies.

Chapter 6: Results

6.1 Overview

A detailed discussion of the results are provided in the following sections. First, the velocity distribution spanning the wind tunnel test section is presented to quantify flow conditions. For this purpose, hot wire anemometry measurements were performed. Turbulence intensity was also calculated to determine the uniformity of the flow at different locations in the test section. Next, the results from the OFI experiment on a flat plate is presented and compared with theory for flows over a flat plate to validate the measurement and analysis methods. The next section discusses calibration of the laminar jet facility used to perform OFI on a flexible membrane. Finally, the results of skin friction measurement on a flexible membrane using OFI are presented. The results show good agreement with theoretical results for flow over a flat plate.

6.2 Hot Wire Anemometry

Hot wire anemometry is a robust technique to measure velocities. The constant temperature anemometer (CTA) wire requires calibration prior to use. For calibration, a manometer was used to read dynamic pressure from the wind tunnel's test section. This known velocity can be used to calculate the local free stream velocity within the test section. The output voltage from the CTA can be related to velocity using King's Law [White, 1974], given by

$$E^2 = A + BU^n, \tag{6.1}$$

where the variables are defined as the average output voltage (E), A and B are constants determined during calibration before the run, U is the velocity, and n is the velocity exponent that is a known constant, n=0.45, per the manufacturer's spec sheet [Fingerson and Freymuth, 1983]. Determining the constant coefficients A and B in Equation 6.1 is done by curve fitting calibration data, as shown in Figure 6.1. With A and B known, the local velocity can be calculated. Figure 6.2 shows a single case of raw velocity data as a function of time during the steady state of the wind tunnel. The frequency and filtering details are discussed in Chapter 3. The recorded fluctuations in velocity show the high frequency fluctuation in the test section. Figure 6.3 shows normal distribution of a selected case with the velocity centering the mean of the data set.

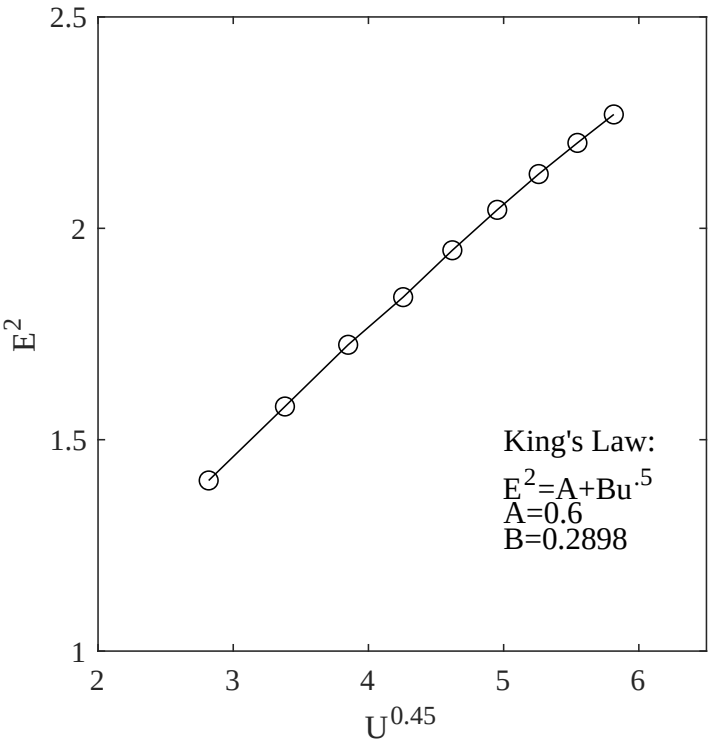

Figure 6.1: Coefficient determination for King's Law.

6.3 Wind Tunnel Characterization

The profile of the wind tunnel is shown in Figure 6.4 where 8 different velocities ranging from $15 > u < 50$m/s were measured at three distinct heights from the base of the test section: 12.7cm (5in), 22.86cm, (9in), and 33.02cm (13in). The $15\frac{m}{s}$ case holds the maximum deviation of the entire data set of $0.437\frac{m}{s}$. The error bars represent the precision error (E_p) of each measurement for a 95% confidence level, and is shown by

$$E_p = \frac{2\sigma}{\sqrt{N}}, \tag{6.2}$$

where σ is the standard deviation of the data set, and N is the number of data points in the data set.

The largest deviation in recorded velocity was $0.4372\frac{m}{s}$ in the $15\frac{m}{s}$ case shown in Figure 6.4. This result shows a uniform velocity profile within the test section that does not vary significantly in the test section. To further quantify the test section velocity profile, turbulence intensity was analyzed. Turbulence intensity provides information regarding the behavior of any unsteady flow present in the test

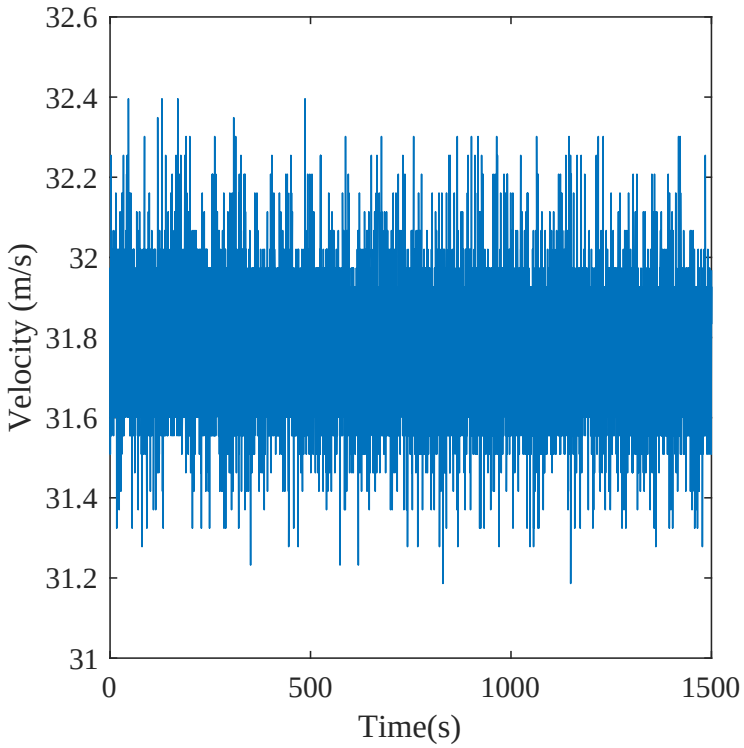

Figure 6.2: Raw velocity data determined using King's Law.

section [Hideharu, 1991]. The turbulence intensity (TI), is given by

$$TI = \frac{u^{'}}{u}, \tag{6.3}$$

where $u^{'}$ is the mean square fluctuation component, and u is the absolute mean velocity [White, 1974, Sentker and Riess, 2000]. Figure 6.5 shows the resulting turbulence intensity profile in the wind tunnel test section.

Turbulence intensity varies from 0.416% to 0.702% depending on velocity and measured location. The selection of the three distinct heights were based on reasonable locations for an experiment being conducted in the wind tunnel. Testing very close to the top or bottom panel is avoided because of boundary layer development on the test section walls. Low fluctuation differences at the center led to the conclusion that the location of the flat plate used for OFI experiments in the test section should be at 22.86cm (9in) from the base. Furthermore, the presence of a steady velocity field reduces systematic error for future measurements in the wind tunnel.

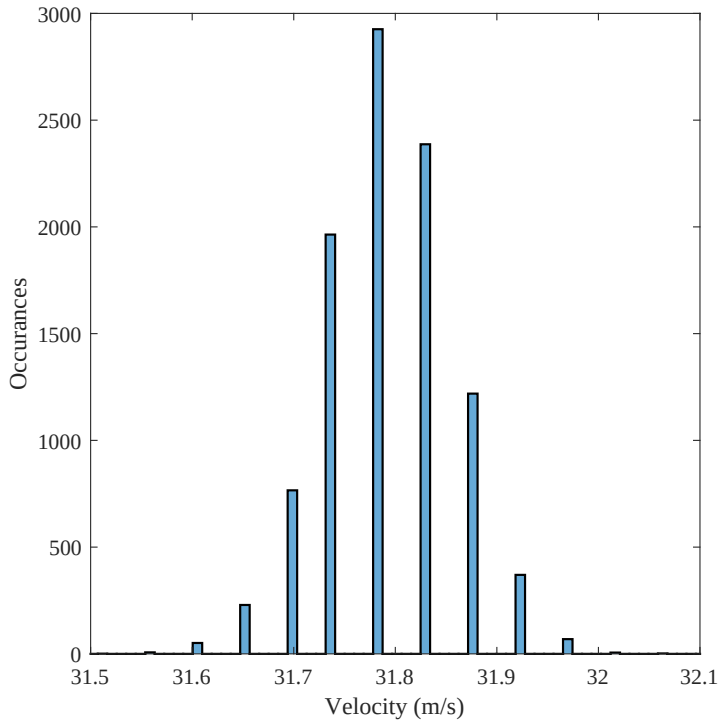

Figure 6.3: Normal distribution for a HWA velocity data set.

6.4 Flat Plate OFI

To validate the oil film interferometry measurement and analysis techniques, OFI experiments were performed on a flat plate. The flat plate experiment was chosen for validation because of the known theory behind boundary layer behavior over a flat plate. Furthermore, there are plenty of studies to compare results with [Tanner and Blows, 1976, Naughton and Hind, 2013, Garrison and Ackman, 1998]. The flat plate experiment performed here spanned the laminar and turbulent boundary layer regimes. Multiple tests were performed at different Reynolds numbers, Re_x, ranging from 4.9×10^4 to 1.6×10^5. The Reynolds number varies as a function of both velocity and distance and is given by

$$Re_x = \frac{\rho U_\infty x}{\mu}, \tag{6.4}$$

where ρ is the air density, U_∞ is the free-stream velocity of the wind tunnel, μ is the dynamic viscosity of air, and x is the fringe distance from the leading edge of the oil as shown in Figure 6.6. C_f for the laminar boundary layer is given by

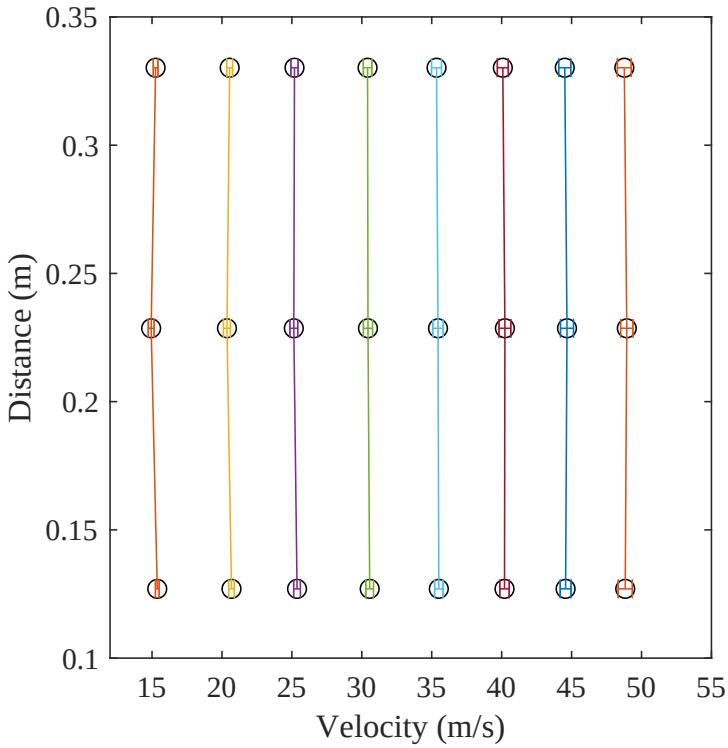

Figure 6.4: Velocity profile of the wind tunnel as a function of height from the base of the test section.

Table 6.1: Flat plate OFI test parameters

T_{atm}(°C)	P_{atm} (kPa)	$\frac{qdt}{\mu}$	Avg. Fringe Spacing (mm)	Velocity ($\frac{m}{s}$)	$Re_{x,avg}$	# of Fringes Analyzed
20.9	100.41	2.25e+06	0.77	16.1	5.00e+04	27
20.8	100.41	2.54e+06	2.99	26.34	7.66e+04	9
21.1	100.41	4.19e+06	3.9	37.26	1.25e+05	17
21.3	100.41	3.61e+06	3.00	49.02	1.62e+05	19

$$C_f = \frac{0.664}{\sqrt{Re_x}}, \tag{6.5}$$

and the turbulent boundary layer can be modeled as

$$C_f = \frac{0.027}{Re_x^{\frac{1}{7}}}. \tag{6.6}$$

The test parameters for each case that were used to estimate C_f, are listed in Table 6.1. An iterative method described in Chapters 2 and 4 was used to estimate C_f. An averaged C_f value of 5 intensity lines over an entire fringe pattern. Figure 6.6 shows a sample case of the 5 intensity lines extracted from

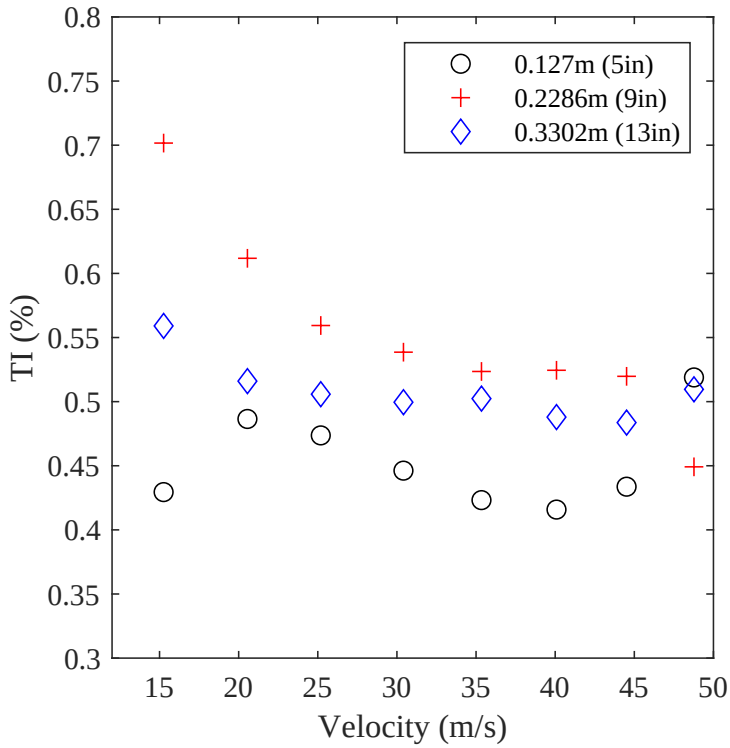

Figure 6.5: Turbulence intensity profile spanning the wind tunnel test section.

the image. Line spacing was dependent on fringe size and varied for each case as the fringe patterns were all slightly different from one another. The cross markings at the bottom of Figure 6.6 are references to convert image coordinates (pixels) to world units (mm), as described in Chapters 2 and 4. Figure 6.7 shows a sample filtered intensity signal, using techniques discussed in Chapter 4, from a line. The critical parameter used to solve for C_f, which is the oil thickness h, is shown in Figure 6.8. Each data point corresponds to a dark or bright fringe.

Figure 6.9 shows the resulting skin friction coefficients along the flat plate. The two turbulent cases agree with turbulent boundary layer theory where $Re_x > 10^5$, with an average deviation of 6.38%. Low free-stream turbulence at these measured locations and a fully developed turbulent boundary layer attribute to the success of these results. The low Reynolds numbers analyzed are expected to agree with the laminar boundary layer theory. However, at these Reynolds numbers, we expect early transition from a laminar to turbulent boundary layer in the presence of free-stream turbulence within the test section. Results of several other studies have shown similar behavior in the boundary layer. [Van Driest and Blumer, 1963, Reshotko, 1994, Garrison and Ackman, 1998].

The one laminar case is in good agreement with theoretical results for a laminar boundary layer.

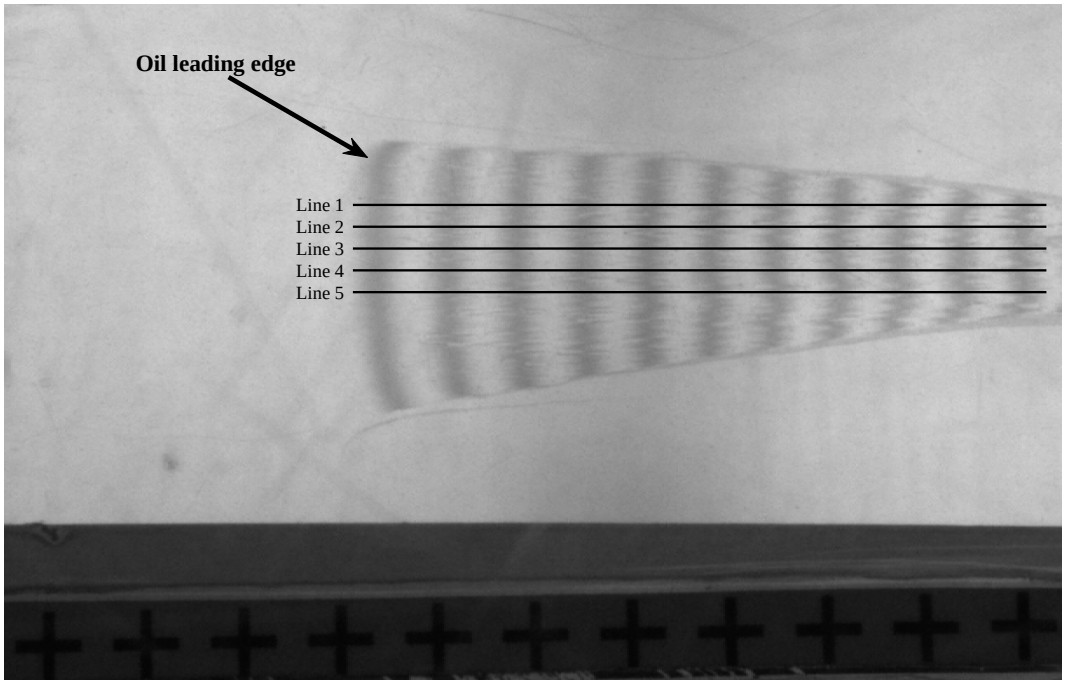

Figure 6.6: Intensity lines that were extracted for pixel intensity analysis.

The average deviation from theoretical results is 22%. This was the lowest operating velocity for these experiments, and as observed in Figure 6.5, corresponds to the highest turbulence intensity.

The case that appears in the transition region in Figure 6.9 is difficult to characterize due to the transition region being random and unpredictable in most cases. However, the transition region is well documented in literature [Munson et al., 2013, White, 1974, Zheng et al., 2019]. C_f experiences a sharp increase after the laminar region before entering the fully turbulent region and gradually decreasing as a function of Re_x, as displayed in the transition region of Figure 6.9. The startup time of the wind tunnel is the time it takes from no flow in the wind tunnel to the time when the flow reaches its steadiest state. At the highest velocity case, the start-up time is $13s$. The images analyzed for each case were taken at $t > 100s$, at which the flow within wind tunnel was in its most steady state for more than $87s$. This accounts for the sharp increase in dynamic pressure that occurs during the wind tunnel start-up time. More Reynolds numbers were explored by increasing velocities in the wind tunnel. The results of the high velocity cases were disregarded due to vibrations in the setup. The fringes did not form well at higher velocities, even with applying more viscous oil with the intent to slow the formation of oil fringes. The fringes formed very quick and essentially covered the area of the plate in under 2 minutes. Therefore, by the time the fringes were fully developed, duration of the wind tunnel's steady state was short, leading

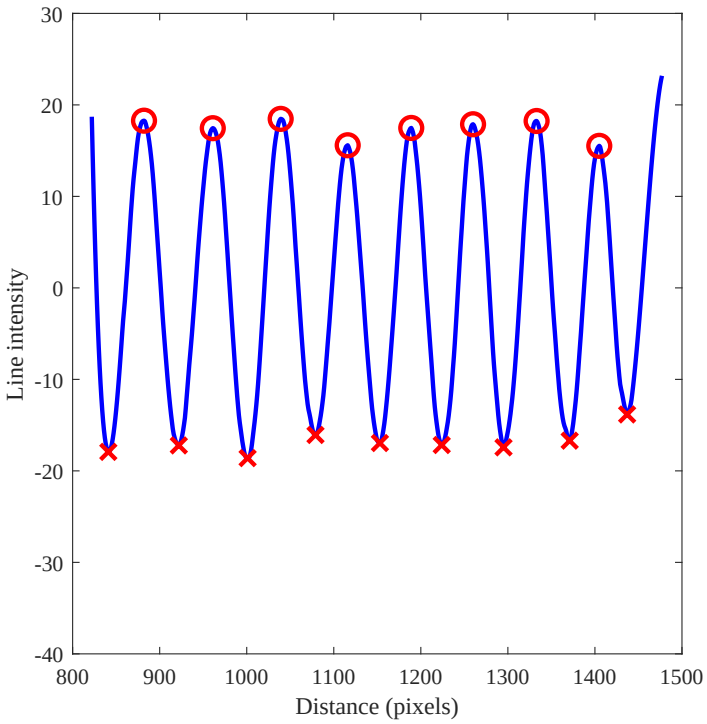

Figure 6.7: Corresponding filtered peak and valley locations as a function of pixel distance for one intensity line.

to a large effect on the pressure increase that occurs during start-up time. Another reason being that the effect of ramping up the wind tunnel in steps when performing tests at various velocities may have had an effect on the uniformity of flow within the test section by the time the higher velocity cases were reached.

6.5 Jet Flow Characterization

To ensure uniform velocity at the exit of the jet, velocity vectors were captured from Particle Image Velocimetry (PIV) measurements. The application of PIV in this study is minimal, and only its direct application will be discussed. For more information on PIV, see [Raffel et al., 1998, Adrian and Westerweel, 2011]. The application for this study was to utilize the combination of PIV instruments to image-map velocity vector data based on change in pixel position over time, at the exit of the jet. The velocity magnitude, U_{mag}, is shown in Figure 6.10. The flow is uniform in the y direction at the leading edge of the flexible membrane, ensuring that flow separation is not present at the junction of the fluid and structure.

The jet facility at EFAL is a motor controlled flow where the known jet exit velocity, U_∞, is represented

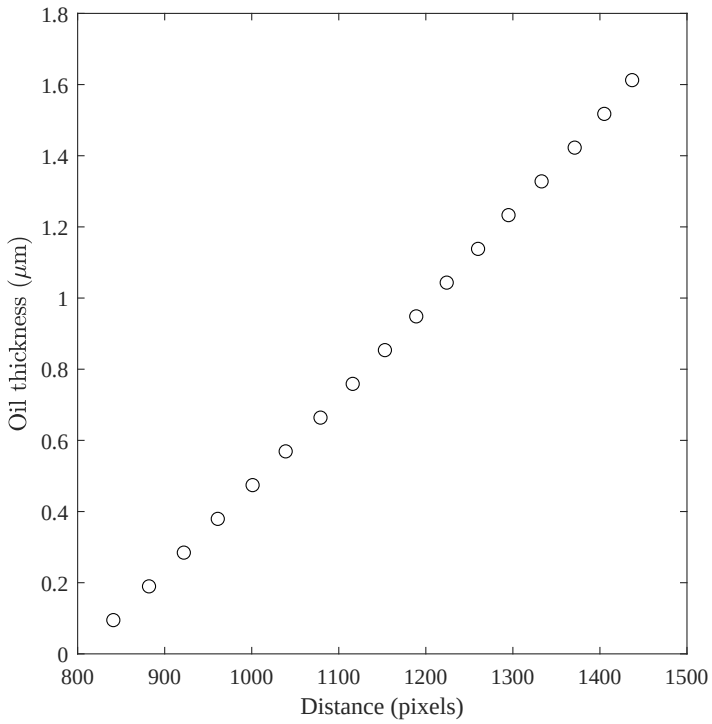

Figure 6.8: Oil height as a function of pixel distance for one intensity line.

by revolutions per minute (RPM) of the motor. To create a common unit for U_∞, the jet was calibrated using PIV. The desired velocities for calibration was done within the bounds of this experiment, meaning the flexible membrane was in a relatively steady position. 500 PIV images were taken for each of the 10 desired velocities. Figure 6.11 shows the 10 calibration points and curve fit, where the jet exit velocity magnitude ($\frac{m}{s}$) is a function of RPM.

6.6 Jet OFI

An analytical solution for skin friction experienced by a flexible membrane subject to flow is discussed here. After validating the OFI experimental procedure and analysis on a flat plate, OFI was performed on a flexible membrane using the jet facility. Experimental results were hypothesized to follow a similar profile to the laminar boundary layer of a flat plate. The shape and extremely thin leading edge allowed for analysis to be coincident with laminar flat plate theory. When the membrane is exposed to a jet exit velocity of more than 12.5 m/s, it begins to flutter at a frequency of up to 20Hz. (More information regarding the fluttering is discussed in Chapter 8). To conduct tests when the membrane was in a relatively steady state, meaning small vibrations were present at the most, cases were selected at jet exit

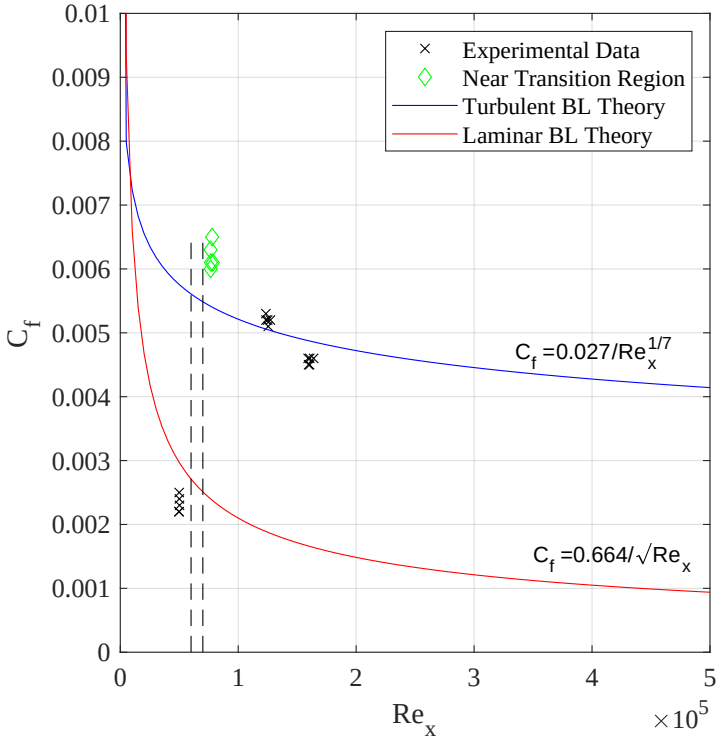

Figure 6.9: Skin friction results from the flat plate experiment. The dashed lines represent the expected transition region.

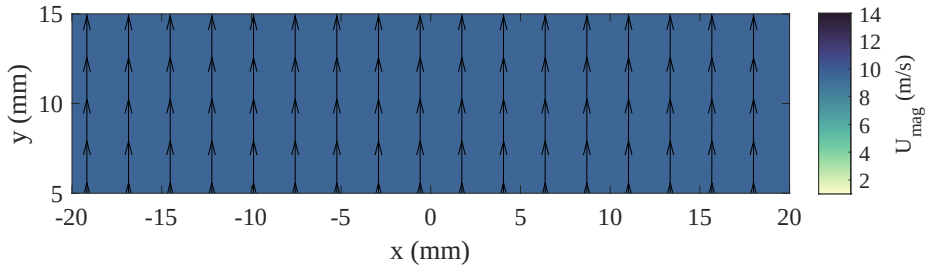

Figure 6.10: Velocity magnitude at the outlet of the jet.

velocities ranging from $4.48\frac{m}{s}$ to $12.1\frac{m}{s}$. Table 6.2 shows the test parameters for OFI on the flexible membrane.

Skin friction results on the flexible membrane are shown in figure 6.12. The experimental results closely follow the theoretical curve for a laminar boundary layer over a flat plate. The average deviation

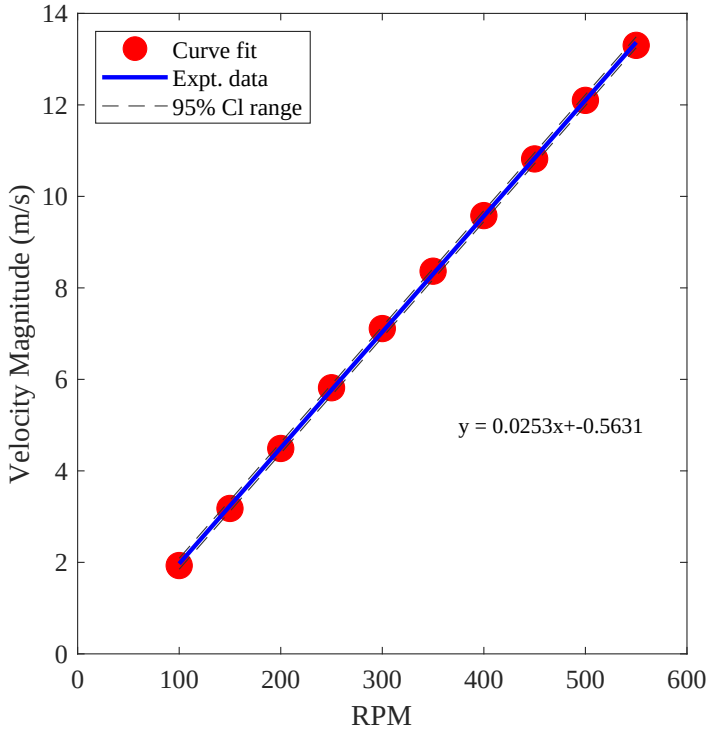

Figure 6.11: Jet facility outlet velocity calibration based on an RPM controller. Shown with curve fit and a 95% confidence level.

from theoretical results is under 8%. At an extremely low Re_x, $9.3 \times 10^3 < Re_x < 1.02 \times 10^4$, the average deviation from theory is 28.7%. This is likely due to the low number of data points produced by the oil fringe at such a low velocity. The pattern had roughly 4 fringes after a run time of over 1400s, whereas the other 3 cases had upwards of 20-25 fringes. After a period of time, small dust particles can collect on the oil that cause the fringes to separate or converge. This leads to problems when assessing the intensity signal of the fringe, thus the test is completed before this occurs.

These results closely agreeing with flat plate boundary layer theory deems high regard to this measurement technique for deriving skin friction on a flexible membrane. In terms of FSI, the mass of the oil

Table 6.2: Flexible membrane OFI test parameters

T_{atm}(°C)	P_{atm} (kPa)	$\frac{qdt}{\mu}$	Avg. Fringe Spacing (mm)	Velocity ($\frac{m}{s}$)	$Re_{x,avg}$	# of Fringes Analyzed
20.9	101.73	7.98e+05	0.88	4.49	9.99e+03	16
20.9	101.73	9.14e+05	0.69	7.11	1.88e+04	17
20.9	101.73	1.66e+06	1.14	9.58	2.58e+04	25
20.8	101.73	2.56e+06	1.59	12.1	3.40e+04	28

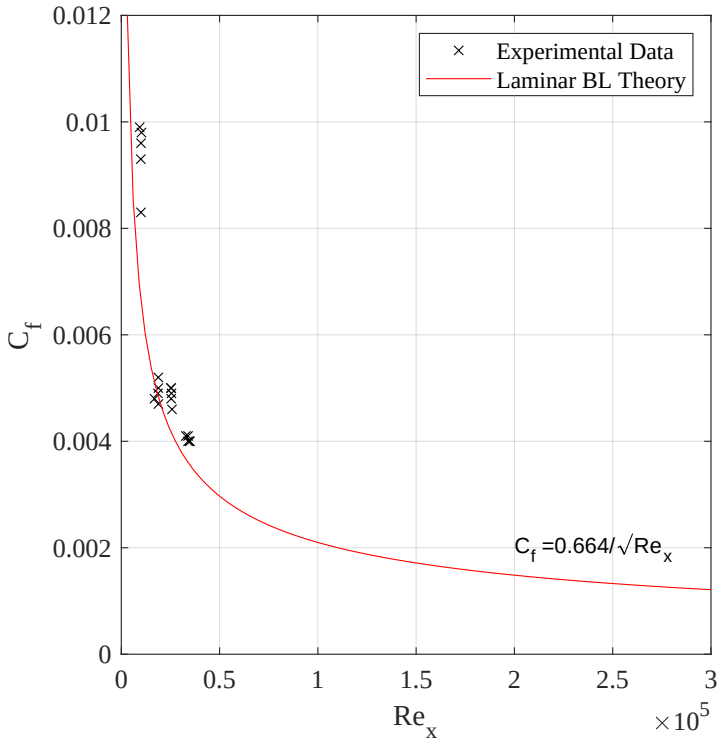

Figure 6.12: Skin friction results from the flexible membrane experiment.

is insignificant to impact the natural behavior of the membrane. Also, the thickness of the oil does not impact the natural behavior of the free-stream velocity.

Chapter 7: Conclusions

The focus of this study was to design, develop and test a robust skin-friction measurement system to quantify the skin-friction coefficients on a flexible membrane. Most traditional methods used for skin-friction measurements are intrusive and may not be feasible to measure skin friction on a thin and flexible membrane. For instance, a MEMS sensor or Stanton tube would influence the characteristics of the boundary layer and thereby altering the flow behavior. Attaching a MEMS sensor would alter the structural properties, even though MEMS sensors are on the order of micro-scale. Furthermore, attaching sensors to a thin membrane could create unbalanced forces and significantly alter the dynamics of FSI behavior.

In order to overcome the challenges of using MEMS sensors for skin-friction measurement, an OFI approach for measuring the skin-friction coefficient was used for this study. OFI is an optical-based skin-friction measurement technique and is non-intrusive. Therefore, an in-house OFI system was designed and developed. The OFI system consisted of a white-light source, a CCD camera system with a frame grabber controlled using a LabView program, and a 532nm optical band-pass filter. The white-light source provided 532nm wavelength light and was used for generating interferometry fringe patterns on a thin oil film. The interferometry fringe patterns were analyzed using an in-house Matlab function to determine skin-friction coefficients.

First, the OFI system was tested for making skin-friction measurements on a flat-plate model in the wind tunnel facility. The results from the wind tunnel testing clearly showed that the in-house designed system was capable of measuring skin friction coefficient and could be used for a range of Reynolds numbers. The skin-friction coefficients on the flat-plate model for the studied Reynolds numbers have an average deviation within 6% of theoretical skin-friction coefficient values. After the system was tested in the wind tunnel, the second phase of this study focused on testing the OFI system to measure the skin-friction coefficient on a transparent flexible membrane in the open jet facility. The in-house OFI system successfully measured the skin-friction coefficient on a flexible membrane for the studied Reynolds number ranges. The measured skin-friction coefficients were less than 8% of the theoretical skin-friction coefficients for flow over a flat plate. This study demonstrated that the OFI technique could be used to measure the skin-friction values on a transparent flexible thin membrane.

Boundary layer theory for a flexible oscillating structure is a complex problem, and researchers have been working on expanding more about the role of instabilities and the impact of viscous drag forces on FSI flutter behavior. Performing OFI to measure skin friction coefficients has provided a new approach to characterizing the wall shear stresses on a flexible membrane. This work has laid the foundation for

future work in which OFI measurements will be taken at a higher Reynolds number regime where different modes of oscillation are observed for the flexible membrane. The next phase of hardware development for the OFI will focus on triggering the camera for a focused image on an oscillating membrane.

Chapter 8: Future Work

8.1 Overview

As stated in Chapter 1, an objective of this study was to lay a foundation for more complex FSI problems regarding skin friction measurements. The development of a program that can take the intensity signal from an image of an oil fringe, and analyze it to the point of skin friction and wall shear stress has been achieved. The experimental setup is valid based on the results agreeing with theory. The expected future work to be conducted at University of Idaho's EFAL is summarized below.

8.2 Turbulent Boundary Layer

In order to model the turbulent boundary layer of an unstable structure, both the boundary layer from the fluid and the boundary layer from the structure must be modeled. The fluid side can be derived from the non-linear Navier-Stokes momentum equation [Temam, 2001]. The structural side can be solved by using the equations of motion for a deforming flag shown in [Paidoussis, 1998]. The non-linear coupling raises concern on how to solve for the pressure term in these equations. Well, the pressure term can be back-calculated on both sides of the flag by deducing the total drag. The total drag is made up of pressure drag and skin friction (or viscous) drag. OFI is the methodology being used to derive the skin friction drag. From the total drag force recorded by a load cell, the friction drag effects can be accounted for from the OFI derivations and thus the pressure component can be solved for.

8.3 Data Acquisition System

Multiple experimental techniques will be combined to perform these measurements. Particle Image Velocimetry will be used to calculate the velocity vectors acting at different locations on the flexible membrane, as well as timing. Hot Wire Anemometry will be used to correlate Von Karman vorticies that occur in the flag's wake region with shedding speed and shearing. The load cell will measure the total force that the membrane is enduring. All of the techniques discussed will have to be triggered and performed in synchronization.

8.4 Advanced Analysis

Large data sets have been collected from PIV in a separate study. Proper Orthogonal Decomposition can be applied to analyze the spatial and temporal behavior of the fluttering membrane. The velocity field data can be reconstructed to better understand the corresponding pressure gradients. If velocity

fields and pressure gradients can be derived, more information about the loads experienced by the fluid and the motion of the flexible membrane can be studied.

References

[Ackerman and Hoover, 2001] Ackerman, J. D. and Hoover, T. M. (2001). Measurement of local bed shear stress in streams using a preston-static tube. *Limnology and Oceanography*, 46(8):2080–2087.

[Adrian and Westerweel, 2011] Adrian, R. J. and Westerweel, J. (2011). *Particle image velocimetry*. Number 30. Cambridge university press.

[Benjamin, 1960] Benjamin, T. B. (1960). Effects of a flexible boundary on hydrodynamic stability. *Journal of Fluid Mechanics*, 9(4):513–532.

[Cunnington et al., 2002] Cunnington, M., Westra, L., Steve, B., Budwig, R., and Elger, D. (2002). Design of a wind tunnel facility for hands on use by beginning engineering students. In *2002 Annual Conference*, pages 7–372.

[Decker and Naughton, 2001] Decker, R. and Naughton, J. (2001). Improved fringe imaging skin friction analysis using automated fringe identification. In *39th Aerospace Sciences Meeting and Exhibit*, page 557.

[Decker, 2002] Decker, R. K. (2002). Viscous drag measurement and its application to base drag reduction. Master's thesis, University of Wyoming.

[Doering and Gibbon, 1995] Doering, C. R. and Gibbon, J. D. (1995). *Applied analysis of the Navier-Stokes equations*. Number 12. Cambridge university press.

[Ehrenstein et al., 2014] Ehrenstein, U., Marquillie, M., and Eloy, C. (2014). Skin friction on a flapping plate in uniform flow. *Philosophical Transactions of the Royal Society A: Mathematical, Physical and Engineering Sciences*, 372(2020):2–13.

[Fingerson and Freymuth, 1983] Fingerson, L. and Freymuth, P. (1983). Ifa 100 system instruction manual. *TSI Incorporated*.

[Garrison and Ackman, 1998] Garrison, T. and Ackman, M. (1998). Development of a global interferometer skin-friction meter. *AIAA journal*, 36(1):62–68.

[Ghouila-Houri et al., 2017] Ghouila-Houri, C., Gallas, Q., Garnier, E., Merlen, A., Viard, R., Talbi, A., and Pernod, P. (2017). High temperature gradient calorimetric wall shear stress micro-sensor for flow separation detection. *Sensors and Actuators A: Physical*, 266:232–241.

[Goza and Colonius, 2018] Goza, A. and Colonius, T. (2018). Modal decomposition of fluid–structure interaction with application to flag flapping. *Journal of Fluids and Structures*, 81:728–737.

[Gyorgyfalvy, 1967] Gyorgyfalvy, D. (1967). Possibilities of drag reduction by the use of flexible skin. *Journal of Aircraft*, 4(3):186–192.

[Hideharu, 1991] Hideharu, M. (1991). Realization of a large-scale turbulence field in a small wind tunnel. *Fluid Dynamics Research*, 8(1-4):53.

[Houghton and Carpenter, 2003] Houghton, E. L. and Carpenter, P. W. (2003). *Aerodynamics for engineering students*. Elsevier.

[Lunte et al., 2018] Lunte, J., Schnepf, C., and SchÃ¼lein, E. (2018). Optical wall shear stress measurements on the leeward side of a delta wing.

[MATLAB, 2021] MATLAB (2021). *version 9.11.0 (R2021b)*. The MathWorks Inc., Natick, Massachusetts.

[Mikhail et al., 2001] Mikhail, E. M., Bethel, J. S., and McGlone, J. C. (2001). Introduction to modern photogrammetry. *New York*, 19.

[Monson et al., 1993] Monson, D. J., Mateer, G. G., and Menter, F. R. (1993). Boundary-layer transition and global skin friction measurement with an oil-fringe imaging technique. *SAE Transactions*, pages 1829–1843.

[Munson et al., 2013] Munson, B. R., Okiishi, T. H., Huebsch, W. W., and Rothmayer, A. P. (2013). *Fluid mechanics*. Wiley Singapore.

[Narasimha and Prasad, 1994] Narasimha, R. and Prasad, S. (1994). Leading edge shape for flat plate boundary layer studies. *Experiments in Fluids*, 17(5):358–360.

[Naughton and Hind, 2013] Naughton, J. and Hind, M. (2013). Multi-image oil-film interferometry skin friction measurements. *Measurement Science and Technology*, 24(12):124003.

[Naughton et al., 2001] Naughton, J. W., Decker, R. K., and Jafari, F. (2001). Automatic fringe detection for oil film interferometry measurement of skin friction. Technical report.

[Naughton and Liu, 2007] Naughton, J. W. and Liu, T. (2007). Photogrammetry in oil-film interferometry. *AIAA journal*, 45(7):1620–1629.

[O'Grady et al., 2009] O'Grady, A., Larger, R., Tiliakos, N., Papadopoulos, G., Modi, V., and Fréchette, L. (2009). A mems sensor for mean shear stress measurements in high-speed turbulent flows with backside interconnects. In *TRANSDUCERS 2009-2009 International Solid-State Sensors, Actuators and Microsystems Conference*, pages 272–275. IEEE.

[Paidoussis, 1998] Paidoussis, M. P. (1998). *Fluid-structure interactions: slender structures and axial flow*, volume 1. Academic press.

[Raffel et al., 1998] Raffel, M., Willert, C. E., Kompenhans, J., et al. (1998). *Particle image velocimetry: a practical guide*, volume 2. Springer.

[Reshotko, 1994] Reshotko, E. (1994). Boundary layer instability, transition and control. In *32nd Aerospace Sciences Meeting and Exhibit*, page 1.

[Sakiadis, 1961] Sakiadis, B. (1961). Boundary-layer behavior on continuous solid surfaces: Ii. the boundary layer on a continuous flat surface. *AiChE journal*, 7(2):221–225.

[Sentker and Riess, 2000] Sentker, A. and Riess, W. (2000). Experimental investigation of turbulent wake–blade interaction in axial compressors. *International Journal of Heat and Fluid Flow*, 21(3):285–290.

[Sheplak et al., 2004] Sheplak, M., Cattafesta, L., Nishida, T., and McGinley, C. (2004). Mems shear stress sensors: promise and progress. In *24th AIAA aerodynamic measurement technology and ground testing conference*, page 2606.

[Son et al., 2016] Son, S.-H., Choi, B.-L., Jin, W.-J., Lee, Y.-G., Kim, C.-W., and Choi, D.-H. (2016). Wing design optimization for a long-endurance uav using fsi analysis and the kriging method. *International Journal of Aeronautical and Space Sciences*, 17(3).

[Squire, 1961] Squire, L. C. (1961). The motion of a thin oil sheet under the steady boundary layer on a body. *Journal of Fluid Mechanics*, 11(2):161–179.

[Takizawa et al., 2013] Takizawa, K., Montes, D., Fritze, M., McIntyre, S., Boben, J., and Tezduyar, T. E. (2013). Methods for fsi modeling of spacecraft parachute dynamics and cover separation. *Mathematical Models and Methods in Applied Sciences*, 23(02):307–338.

[Tanner, 1979] Tanner, L. (1979). Skin friction measurement by viscosity balance in air and water flows. *Journal of Physics E: Scientific Instruments*, 12(7):610–619.

[Tanner and Blows, 1976] Tanner, L. and Blows, L. (1976). A study of the motion of oil films on surfaces in air flow, with application to the measurement of skin friction. *Journal of Physics E: Scientific Instruments*, 9(3):194–202.

[Temam, 2001] Temam, R. (2001). *Navier-Stokes equations: theory and numerical analysis*, volume 343. American Mathematical Soc.

[Trilling and Häkkinen, 1955] Trilling, L. and Häkkinen, R. (1955). The calibration of the stanton tube as a skin-friction meter. In *50 Jahre Grenzschichtforschung*, pages 201–209. Springer.

[Van Driest and Blumer, 1963] Van Driest, E. and Blumer, C. (1963). Boundary layer transition-freestream turbulence and pressure gradient effects. *AIAA journal*, 1(6):1303–1306.

[Vandenberghe et al., 2006] Vandenberghe, N., Childress, S., and Zhang, J. (2006). On unidirectional flight of a free flapping wing. *Physics of Fluids*, 18(1):014102.

[Vitug, 2020] Vitug, E. (2020). Hypersonic inflatable aerodynamic decelerator (hiad-2).

[White, 1974] White, F. (1974). Viscous fluid flow. *New York, New York*.

[White, 2011] White, J. C. (2011). High-frame-rate oil film interferometry.

[Winter, 1979] Winter, K. (1979). An outline of the techniques available for the measurement of skin friction in turbulent boundary layers. *Progress in aerospace sciences*, 18:1–57.

[Zheng et al., 2019] Zheng, W., Ruan, S., Yang, Y., He, L., and Chen, S. (2019). Image-based modelling of the skin-friction coefficient in compressible boundary-layer transition. *Journal of Fluid Mechanics*, 875:1175–1203.

[Zilliac, 1996] Zilliac, G. C. (1996). Further developments of the fringe-imaging skin friction technique. Technical report.